Lee Davison Dennis E. Grady
Mohsen Shahinpoor
Editors

High-Pressure Shock Compression of Solids II

Dynamic Fracture and Fragmentation

With 527 Illustrations

Springer

CHAPTER 2

Microstructural Aspects of Dynamic Failure

Anna K. Zurek and Marc André Meyers

2.1. Introduction

The term dynamic failure is used to distinguish special characteristics of failure of materials subjected to dynamic loading. The major feature that differentiates dynamic failure from quasi-static behavior is the presence of stress waves. These waves arise due to the applied load or due to the stresses released from a crack tip at fracture. Several phenomena are particularly relevant to dynamic failure, including:

1. Rapid crack propagation. The velocity of the crack can approach the shock wave velocity; the Rayleigh velocity is widely accepted as the limiting velocity, but it is rarely achieved in real materials, where the maximum values are closer to 1000 m/s [Ravi-Chandar and Knauss (1984a,b); Zehnder and Rosakis (1990)].
2. Fast nucleation, growth, and coalescence of voids. The rapid rate of loading makes the independent nucleation and growth of microvoids possible.
3. Shear band formation: localization of plastic deformation in a narrow region takes place when thermal softening is more pronounced than strain and strain-rate hardening combined. The adiabaticity, or quasi-adiabaticity of the process due to high-strain-rate deformation enhances the propensity for this response. Shear bands often lead to failure by separation of the two sides of material along the band.

Dynamic failure is of considerable importance in several practical applications including crack arrest in engineering structures, fracture plane control in blasting, fragmentation in mining, meteorite impact of space structures, planetary impact or crash worthiness of vehicles and structures. Finally, the military applications of importance are the fragmentation of bombs and shells, the breakup of projectiles, and penetration and fracture of armor.

A good example of the different phenomena associated with the dynamic response of a material can be illustrated by the impact of a projectile against a target. Figure 2.1 captures several important dynamic events associated with such an impact. At the impact surface, as well as throughout the target,

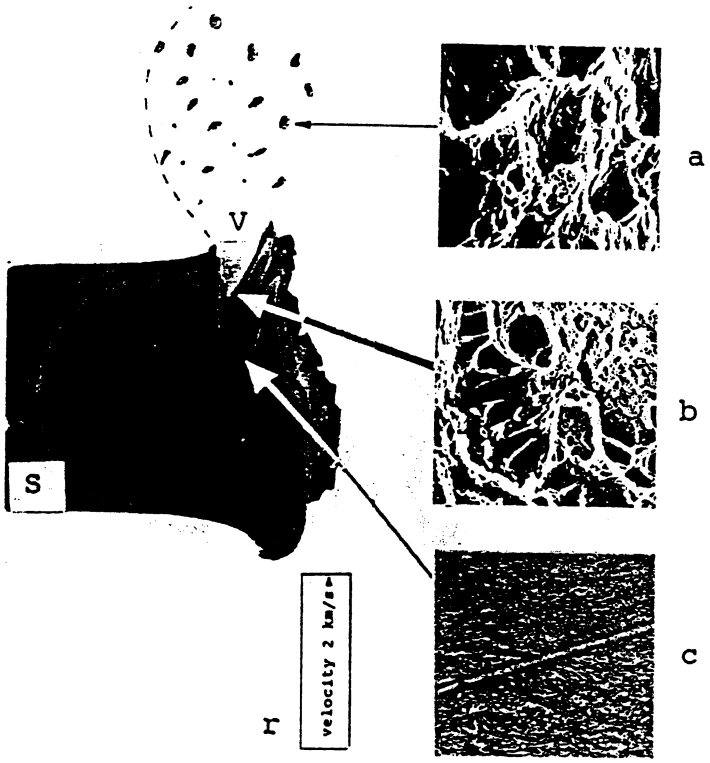

Figure 2.1. A penetration experiment showing important dynamic events. Rolled homogeneous armor steel s, penetrated with a rod r (schematically represented). Opposite the impact surface is a large cavity created by ejection of a cloud of debris. An example of an actual fracture surface of one debris particle is shown in insert a. Insert b shows the fracture surface of the spall cavity. The micrograph of an adiabatic shear band is shown in insert c. [From Zurek (1989)].

one usually observes dynamic deformation events such as shock-wave strengthening in the form of a significant increase in the dislocation density or twinning and other forms of deformation (microbands, slip bands) especially in metals. In other words, the shock wave, if of sufficient amplitude, produces substructural changes in the target. The shock wave can affect the mechanical properties, such as increasing the flow stress, thereby generally decreasing the ductility, and can therefore promote subsequent fracture.

Pressure-induced phase transformations (such as α to ε transition in steels, occurring at about 13 GPa) can also play an important role in changing the response of the material.

In many materials, as the strain rate increases due to the increasing impact velocity, the local temperature increases due to the heat generated from the deformation accumulation; this, in turn, may lead to a localization of the deformation to a narrow portion of the sample. This phenomenon is commonly known as *shear banding*. Shear bands play a very important role in dynamic fracture and fragmentation processes.

Spalling, on the side opposite the impact surface in Fig. 2.1, occurs due to

the tensile stresses generated by the interaction of two release waves, one incoming from the free surface of the projectile and the other reflected from the back free surface of the target. If the tensile stress so generated is higher than the dynamic strength of the target, fracture processes in the sample will be initiated. Whether spall is complete or incipient depends on the duration of the pulse as well as the peak shock amplitude. The thickness of the ejected piece from the back of the target will correspond roughly to the thickness/length of a projectile under simple one-dimensional loading. Spalling will produce release waves at the newly created internal surfaces. More complex loading situations can generate internal stresses in the material and promote fragmentation in the spalled portion of the target.

Another type of dynamic fracture (not shown in Figure 2.1) may occur during the explosion of bombs or shells, and this can be represented by the expanding ring technique. In this technique, the hoop strains generated in the explosively expanding ring dynamically fragment the ring. The fracture occurs at the points of weakness in the material corresponding to the internal or external flaws of the ring. The size and the distribution of the fragments created in the expanding ring experiment depend on the flaw strength, the relative position of defects, and release wave propagation velocity as well as the microstructure of the material.

This chapter focuses on the microstructural aspects of dynamic failure. The mechanics of stress-wave propagation, crack, and shear-band formation were intentionally left out and only very schematic physical pictures of the phenomena are presented. Emphasis is placed on the microstructural effects (grain size, dislocation mechanisms, twinning, shock modification, heat treatment effects, and composition effects) and the primary source of information is the work carried out by the authors and co-workers. Therefore, many significant research efforts are not discussed here, for the sake of conciseness. Since another entire section of this book deals with fragmentation, this important topic is left out.

This chapter is divided into three sections, in addition to the introduction: Section 2.2 (Dynamic Fracture), Section 2.3 (Adiabatic Shear Instability), and Section 2.4 (Stress-Wave Effects in Ceramics and Rocks). Each section is divided into subsections dealing with specific methods of approach or materials.

2.2. Dynamic Fracture

2.2.1. General Description of Phenomena

Dynamic (high-velocity) crack propagation has unique aspects that differentiate it from quasi-static fracture. The main differences are:

a. There is a limiting crack velocity, as stated in Section 2.1. For a detailed treatment the reader is referred to Freund (1990). The analyses that led to limiting crack velocity are due to Broberg (1960), Craggs (1960), and

Freund (1972, 1973, 1974). The physical explanation for this effect is simple. Energy has to be delivered to the tip of the crack to drive it. Most of this energy travels along the crack surfaces, as waves [in a way analogous, but opposite to the energy of an earthquake, most of which is transported away by surface (Rayleigh) waves]. When the crack velocity approaches the Rayleigh wave velocity, it becomes more and more difficult to provide energy to its tip, and therefore this velocity reaches a plateau. Zehnder and Rosakis (1990), and Ravi-Chandar and Knauss (1984a,b) measured maximum velocities in real materials (a polymeric resin and a high-strength steel) and found that they were approximately 500 and 1200 m/s, respectively. This is approximately 50% of the Rayleigh speed. In real materials, grain boundaries, texture, differences between grain sizes, and other effects tend to slow the rate of extension of cracks.

b. At a sufficiently high velocity, there is a tendency for cracks to bifurcate, thereby lowering the overall energy of the system. Thus, quasi-static failure tends to produce one large crack while dynamic failure produces many small fragments.
c. The fracture toughness and yield stress of materials are strain-rate dependent.

Failures by crack and void nucleation, growth, and coalescence occurring dynamically are called brittle and ductile fracture, respectively. Dynamic fracture occurs in a variety of loading situations, not all of which involve stress wave propagation. For instance, a statically loaded system can generate a dynamic fracture event because a crack that grows initially at a low velocity is exposed to an increasing stress intensity factor as its length increases. Thus, the driving energy increases. Steel can undergo a ductile-to-brittle transition as the velocity reaches a critical value. Thus, the crack will accelerate even further by the lowering of the toughness: brittle toughness is generally less than ductile toughness.

For research purposes, a variety of experimental configurations are used to produce dynamic fracture and some of these are:

a. spallation experiments
b. expanding ring experiments
c. tensile stress wave propagation through pre-cracked specimens.

Since most of the experimental results described here are based on spallation experiments, this method will be described in detail.

Spallation, as a dynamic fracture process, occurs in a material due to tensile stresses generated by the interaction of two release (rarefaction) waves. Figure 2.2 is used here to help elucidate the spallation process.

The left-hand side of the diagram represents the projectile, while the right-hand side represents the target. At time $t = 0$, the projectile impacts the target. Elastic waves are emitted into the projectile and the target; they are

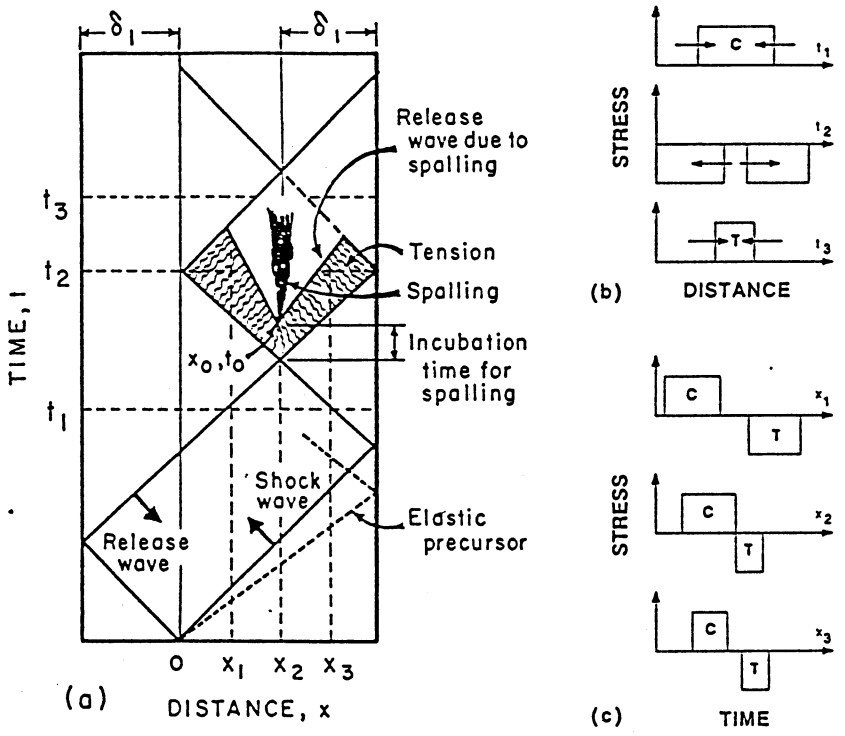

Figure 2.2. Distance–time plot for impact of projectile on target showing spalling induced by tensile stresses.

subsequently followed by a plastic wave. In the plot, the inverse of the slope of the diagonal lines gives the velocities of the waves. It can be readily seen that the elastic precursor has a higher velocity than the plastic shock wave. The elastic and plastic waves encounter the free surfaces of the target and projectile, and they reflect back. The regions in tension and compression are shown. The elastic precursor in this schematic is assumed to be small with respect to the total pulse amplitude. Spalling is dependent on both the amplitude and duration of the tensile pulse. If the tensile pulse is of a sufficient magnitude, spalling will occur. Spalling will produce release waves at the newly created internal surfaces which alter the subsequent configuration of pulses. If the projectile and target are of the same material, the distance of the spall from the back free surface is roughly equal to the thickness of the projectile, δ_1. The travel time of the wave in the flyer plate determines the duration of the compressive wave in the target and this establishes the thickness of the spalled layer.

Stress vs. distance plots at different times and stress vs. time plots at different positions are also shown in Figure 2.2. Multiple spalling is produced when a triangularly shaped pulse is reflected from the back free surface and has an amplitude substantially higher than the critical stress required for fracture. The shape of the pulse determines the distances be-

tween the consecutive spall planes. The spalling process repeats itself until the stress value of the wave has been reduced to less than the critical stress for spall. Spalling experiments generate a multitude of microcracks or microvoids which grow independently and coalesce.

2.2.2. Ductile and Brittle Spall Fracture in Iron and Steels

The majority of shock-spall studies have concentrated on investigating the dynamic fracture and shock strengthening of annealed or stress-relieved metals and alloys [Leslie (1981), Murr (1981)]. Few studies have explored the shock response of materials possessing a pre-existing dislocation substructure formed via heat treatment, quasi-static deformation, or prior shock loading [Gray (1993)]. Iron and steels undergo the reversible, α to ε allotropic phase transformation which occurs at approximately-13 GPa, which poses an additional complication in understanding the dynamic behavior in these materials. Above 13 GPa pressure, the spall morphology and the measured spall strength of iron and alloyed steel changes drastically. The reversible phase transformation, α to ε (during loading above the 13.1 GPa) and back to α (during unloading below 9.8 GPa), has been linked to a change in the mode of fracture from brittle (below the 13 GPa applied stress) to ductile (above the 13 GPa applied stress) and the change from rough to smooth topography at this spall surface, respectively [(Erkman (1961), Banks (1968), Barker and Hollenbach (1974), Ivanov and Novikov (1961), Balchan (1963), Meyers et al. (1980), Meyers and Aimone (1983)].

In spall fracture it is difficult to consider the separation of nucleation and propagation events. In the brittle regime, at lower pressures, cleavage is influenced by the local hydrostatic pressure [Teirlinck et al. (1988)]. Thus, in the spall process the fracture occurs under triaxial tension. As the superimposed hydrostatic tensile pressure increases with shock pre-stress, the spall strength of the material decreases.

The question arises as to why there is such a pronounced change in the mode of fracture in iron and steels associated with the phase transformation, as shown in Figure 2.3.

Several studies have investigated this problem. Erkman (1961), Banks (1968), and Barker and Hollenbach (1974) have proposed that formation of a smooth spall is related to the existence of a rarefaction shock and a sudden rise in a tensile stress pulse occurring in a very narrow region. Therefore, the fracture region is very localized [Meyers and Aimone (1983) and Zurek et al. (1992)]. Figure 2.4 shows a smooth spall produced above 13 GPa.

In the case of a spall below the phase transformation pressure (< 13 GPa), the tensile stress pulse increases at a slower rate, allowing for the deformation to occur in a wider region and thus leading to the formation of a rough spall surface, as in Figure 2.5.

The spall strength of 4340 steel was found to be independent of pre-shocks

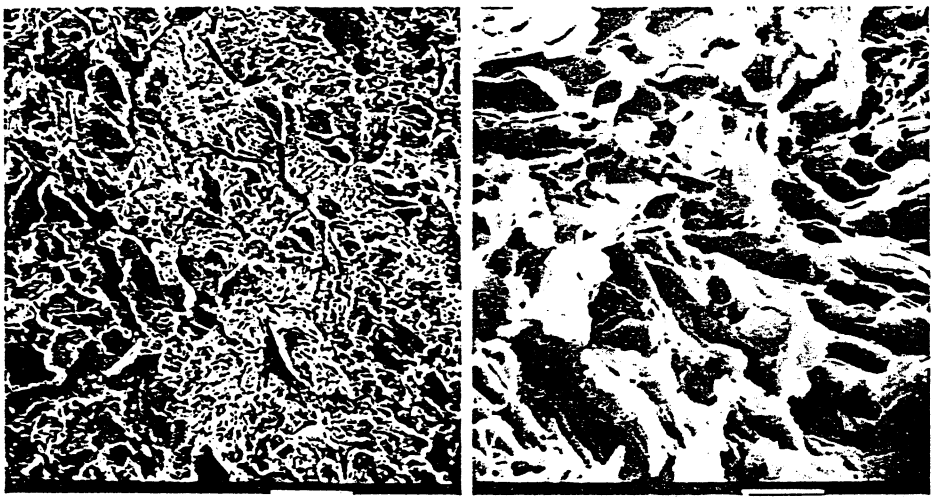

Figure 2.3. Ductile (a), and brittle (b), fracture in 4340 steel. [From Zurek et al. (1990)].

from 10 GPa and 15 GPa in the brittle regime (Zurek et al. (1992)]. This suggests that the fracture process in this material in the brittle regime is dynamic and therefore independent of work hardening and damage induced by such pre-shock. The pre-shock of 15 GPa (above the phase transformation pressure) decreased the spall strength of the 4340 steel in the ductile regime.

An explanation proposed by Zurek et al. (1992) was that the microstruc-

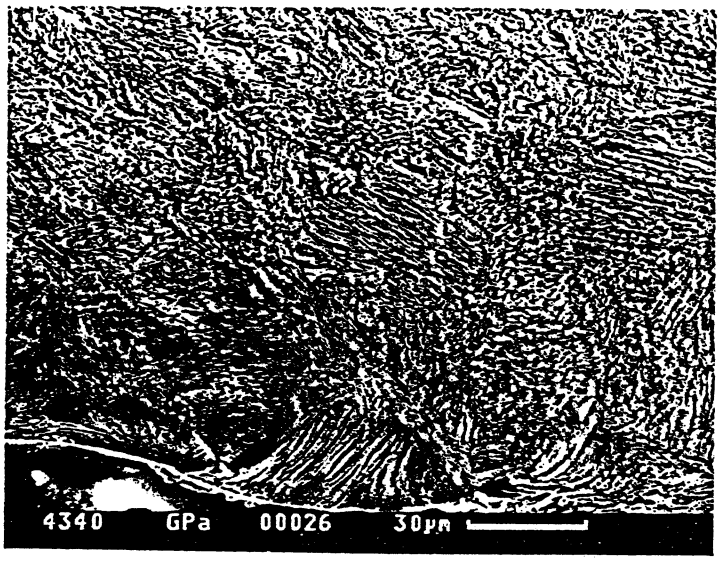

Figure 2.4. Smooth spall in 4340 steel at 15 GPa shown here as an etched cross section, where spall plane is at the bottom of the picture. [From Zurek et al. (1990)].

ture refinement and local deformation due to the phase transformation may create a large number of nucleation sites smaller than the original grains and promote ductile fracture. It is well known [e.g., Meyers and Chawla (1984)] that the ductile-to-brittle fracture transition point can be shifted by grain refinement or by an increase in the strain rate. Also, a sudden local increase in temperature, prompted by the thermodynamics of the phase transformation and combined with a high strain rate localized in a very narrow region, may be an additional reason for the ductile failure mode at a high stress amplitude. Zehnder and Rosakis (1990) used an infrared method to measure the local temperature increase in the vicinity of dynamically propagating cracks in 4340 steel. Their experimental data show that a temperature increase of up to 465°C may occur at the tip of a dynamically propagating crack in 4340 steel, and that the region of intense heating (>100°C) may extend to as much as a third of the active plastic zone size. Others have shown that a temperature increase of 300°C in Armco iron [Curran (1971)], or in low carbon steel [Zurek et al. (1990)], deformed at a strain rate of approximately $10^4\ s^{-1}$, is sufficient to promote ductile fracture even when the spall pressure is far below that necessary for the α to ε phase transformation. However, this temperature is above the dynamic fracture toughness corresponding to the ductile-to-brittle transformation temperature promoting void growth and coalescence. It was proposed by Zurek (1992) that either the substructure modifications due to phase transformation or the local temperature increase may raise the stress for brittle fracture above the peak stress level and promote ductile, smooth spall fracture.

The other observation was that the spall strength in the ductile regime is

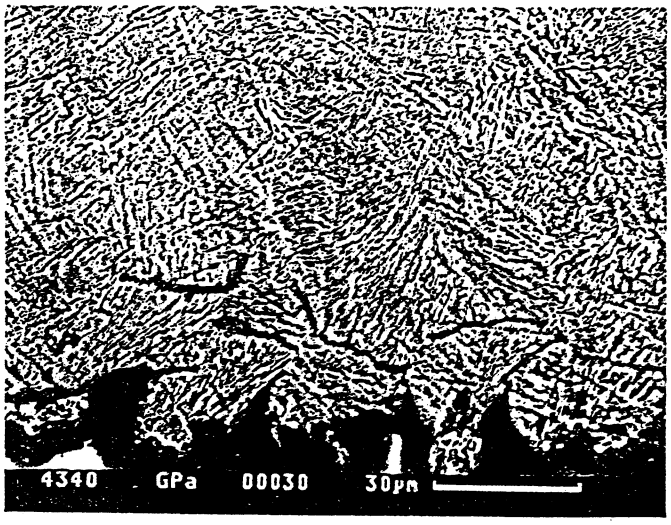

Figure 2.5. Rough spall in 4340 steel at 10 GPa shown here as an etched cross section, where spall plane is at the bottom of the picture. [From Zurek et al. (1990)].

decreased by shock pre-strain. This is consistent with the above hypothesis, because shock pre-straining increases the flow stress and decreases the hardening capacity. These two effects aid the ductile fracture process in spalling and thus lower the spall strength.

Meyers and Guimaraes (1976) found that tensile pulses can generate martensite in austenitic iron–nickel alloys. The effect was used by Thadhani and Meyers (1988) to obtain fundamental kinetic data on martensitic transformation. Dremin et al. (1992) established that the martensitic transformation in the spall region enhances the spall strength of austenitic stainless steel (18/8). This martensitic transformation produces a stress relaxation which results in an anomalous increase in the spall strength of these steels in the 14–18 GPa range.

2.2.3. Spalling in Copper: Microstructural Effects

In this section we will discuss two specific dynamic fracture processes in copper (used here as a model material) and their dependence on the microstructural aspects: (a) tensile fracture under dynamic uniaxial stress conditions (expanding ring experiment); and (b) spalling under dynamic uniaxial strain. Catastrophic failure in an expanding ring is preceded by a large amount of homogeneous plastic strain and little void growth occurs until the latter stages of necking, where void growth and coalescence are responsible for the material fracture. In spalling, void nucleation and growth dominate the tensile plastic flow process from the very beginning and the critical void volume fraction is necessary for ductile spall fracture to occur [Curran, Seaman, and Shockey (1987)]. These observed differences are due to entirely different

tensile stress states in the two cases. Under conditions of uniaxial stress (expanding ring test), voids are subject to a nearly uniaxial stress field. Hence, homogeneous plastic strain dominates the flow process in the early stages. It is assumed that the void growth is nonexistent [Johnson (1981)]. Under conditions of dynamic uniaxial strain (spall test) the principal stress components differ by the flow stress, and thus the voids are subject to a nearly isotropic tensile stress field and void growth dominates all stages of the fracture process [Curran, Seaman, and Shockey, (1987), and Johnson (1981)].

The spall strength of copper and ductile fracture morphologies obtained in an expanding ring test and the symmetric spall test were studied by Zurek et al. (1988). In an expanding ring test the grain size in copper samples varied from 10 to 150 μm. The number of fragments generated in the electromagnetically expanded copper rings did not vary strongly with grain size [Gourdin (1987)], but were dependent on the distribution of random physical imperfections which served as nucleation sites for failure. However, the final cross section of the necked region was found to be grain size dependent (Figure 2.6a and b). The smaller grain size material revealed a larger cross sectional area and a larger number of voids per fracture surface area. In the large grain size material, void density was very low and coalescence occurred only in the latter stages of the fracture process.

The homogeneous plastic deformation preceding fracture was not accompanied by significant void growth.

The microstructure scale and purity play an important role in the spall morphology. In contrast to the expanding ring test, void growth and coalescence precedes the fracture process and are necessary elements for fracture in ductile materials [Curran, Seaman, and Shockey (1987)]. Zurek et al. (1988) found that the spall strength of copper can vary depending on the purity and grain size. They measured the lowest spall strength in the large grain ETP (low purity) copper and the highest strength in the small grain size OFHC (high purity) copper.

Figures 2.7a and b show the fracture surfaces obtained in ETP copper of 40 and 200 μm grain sizes. The inclusion particles (copper oxides), serve as void nucleation sites and therefore the spall is void growth controlled. The differences in the spall strength in this material (listed in the figure caption) are the result of the differences in the grain size.

A homogeneously nucleated transgranular spall fracture was found in OFHC small grain size copper (40 μm), as shown in Figure 2.8.

It was suggested [Stevens, Davison, and Warren (1972) and Zurek et al. (1988)], that voids nucleated on the cross slip planes of the edge dislocations, slipping along the $\langle 111 \rangle$ plane of the cube faces. In a large grain size OFHC copper (200 μm), the nucleation was intergranular, as in Figure 2.9.

It was proposed that in the case of a pure material that spall is nucleation controlled and therefore requires more energy and thus the higher spall strength measured. The spall strength differences listed for OFHC copper

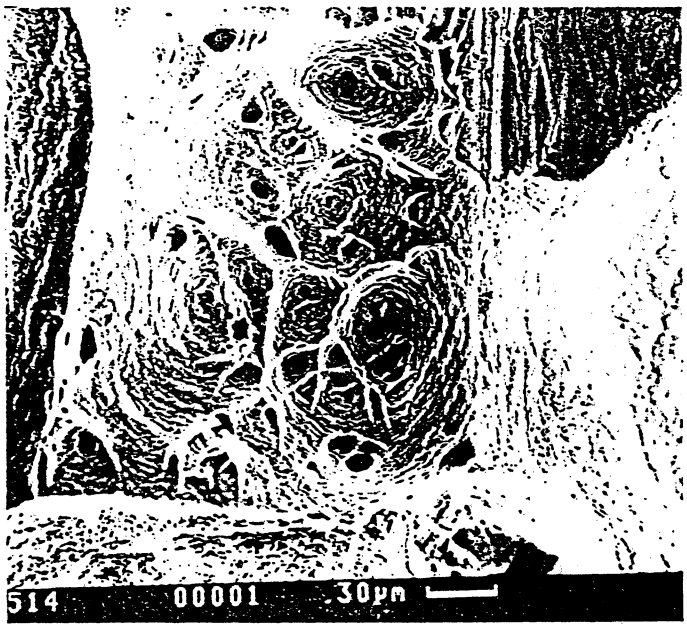

(a)

(b)

Figure 2.6. Voids in expanding ring experiment: small grain size (a), large grain size (b). [From Zurek et al. (1988)].

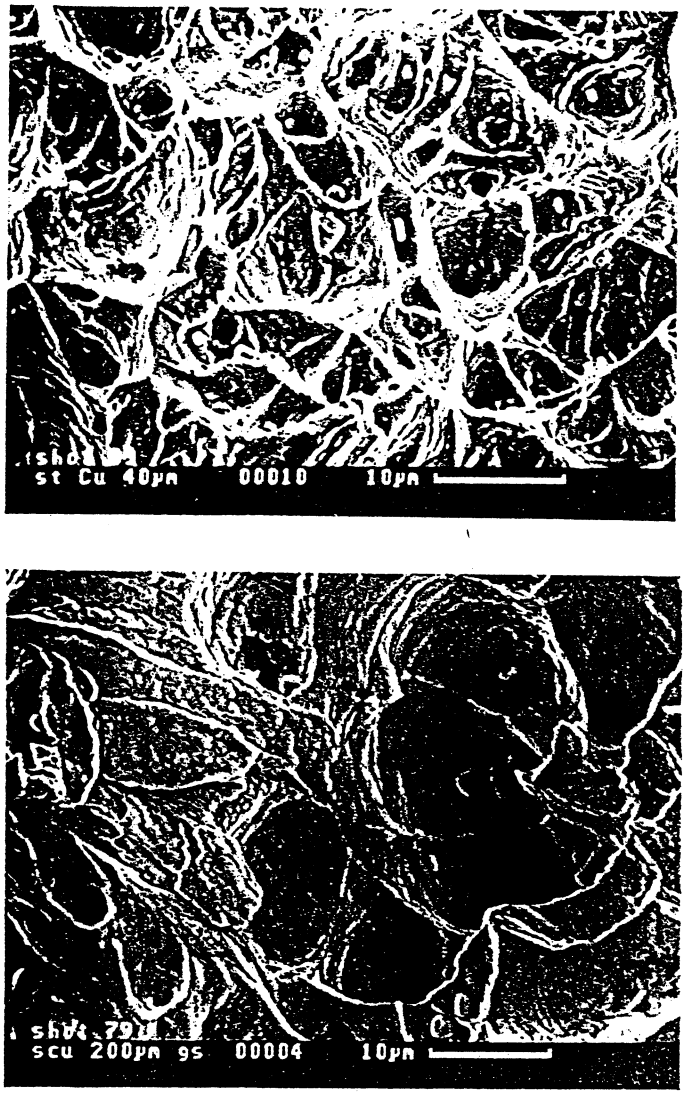

(a)

(b)

Figure 2.7 Fracture surfaces, ETP copper 40 μm. (a) Spall strength -1.5 GPa 200 μm. (b) Spall strength -0.4 GPa. [From Zurek et al. (1988)].

are a result of the change in the mode of fracture from intergranular for l grain size material to transgranular voiding in small grained copper.

Christy, Pak, and Meyers (1986) subjected copper with grain size of 2(and 250 μm to spalling and determined the void volume fraction and ir tion sites. The metallurgical condition (grain size, purity, and pre-defo: tion) was found to have remarkable effect on the spall strength. The rel: spall strength of the specimens did not correlate with their hardne Whereas the 250 and 90 μm specimens exhibited void nucleation at the g boundaries, and as a consequence a ductile intergranular fracture, the 2(grain size and rolled specimens exhibited void nucleation in the interi(

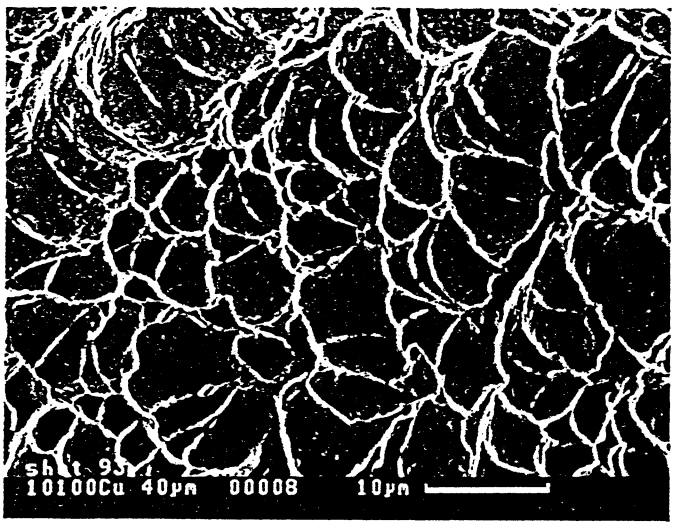

Figure 2.8. Homogeneous nucleation in OFHC copper 40 μm grain size. Spall strength -2.4 GPa. [From Zurek et al. (1988)].

grains. Figure 2.10 shows the differences in void volume fraction observed in the specimens for different metallurgical conditions and at different stress levels. The lower purity (99.5%) copper exhibited a noticeably lower spall strength (more spall damage) than the higher purity (99.99%) copper. The former is the "momentum trap" material marked in Figure 2.10. The explanation for this is simple: the second-phase particles provided easy nucleation sites for voids. The rolled material showed a significantly higher resistance for spalling. Statistical measurements were made and they indicated the following fraction of voids nucleated at grain boundaries:

large grained copper (250 μm)	77%
medium grained copper (90 μm)	65%
small grained copper (20 μm)	30%
rolled copper	49%

The initiation of voids at grain boundaries can be explained by the concentration of impurities at these regions, providing heterogeneous nucleation sites. The larger grain size specimens have a lower interfacial area per unit volume, S_v ($S_v \sim 6/D$; D is a grain diameter). Thus impurities are more severely segregated in these specimens, leading to more pronounced grain boundary failure. Figure 2.11(a) shows a grain-boundary void; markings on the optical micrograph are slip-band traces. Figure 2.11(b) shows a transmission electron micrograph (taken at an accelerating voltage of 1 MeV) of an elongated void. A high concentration of dislocations is noticeable around this void, which has a length of ~ 5 μm. This high dislocation density is the direct consequence of plastic strain necessary to create the void.

Kanel et al. (1992) determined the spall strength of copper mono- and

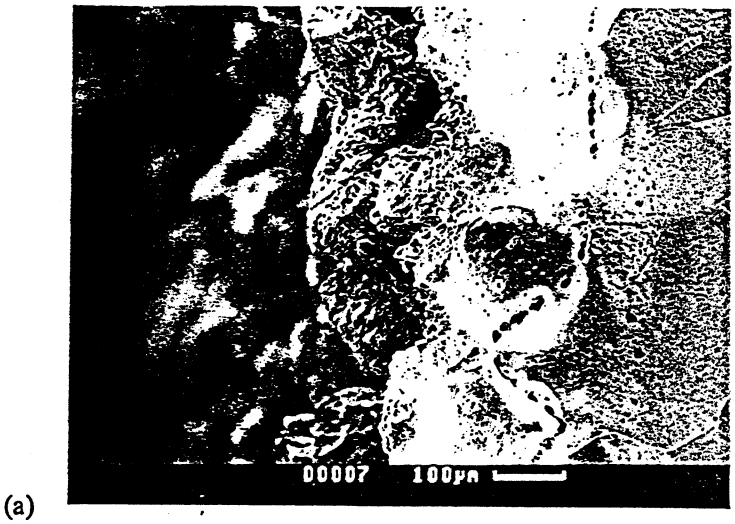

(a)

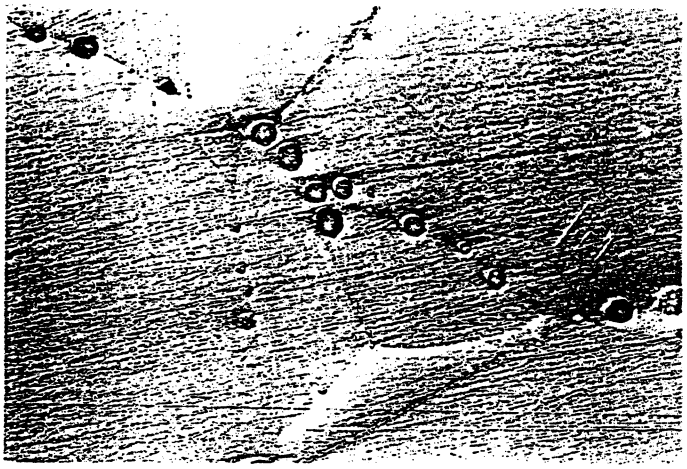

(b)

Figure 2.9. Grain boundary nucleation in OFHC copper 200 μm grain size. Spall strength -1.5 GPa. [From Zurek et al. 1988 (a) and Christy, Pak, and Meyers (1982) (b)].

polycrystals and found, surprisingly, that the former had a significantly higher strength than the latter. Polycrystalline copper had a spall strength of ~ 1.36 GPa; on the other hand, monocrystalline copper had a spall strength of ~ 4.6 GPa. This is in contrast with the quasi-static strength of these materials. The explanation for this anomalous behavior lies in the absence of grain-boundary void nucleation sites for the monocrystalline copper.

2.2.4. Dynamic Fracture in Tungsten and Tungsten alloys: Heat Treatment and Alloying Influence

The spall strength of intrinsically brittle tungsten changes dramatically with both heat treatment and alloying. In recent years several investigators have studied the static and dynamic properties of tungsten alloys in sintered and

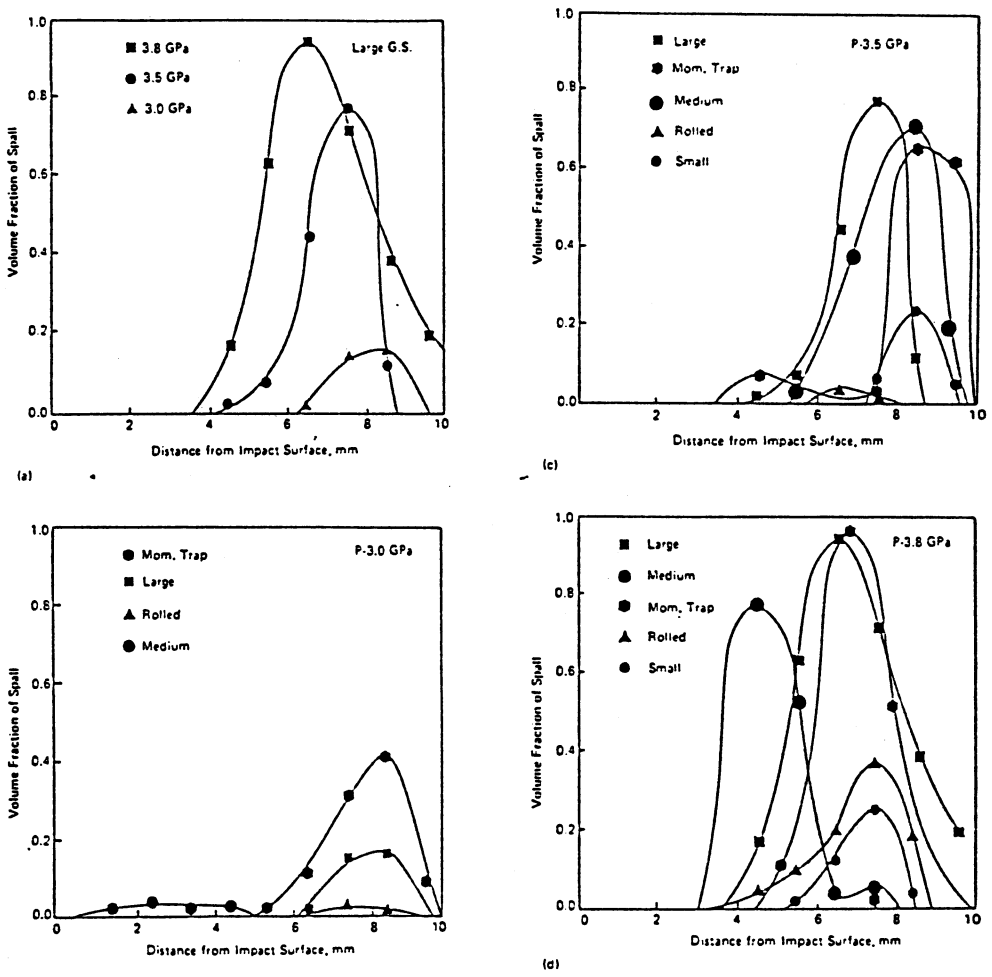

Figure 2.10. Volume fraction of voids formed during spalling experiments in copper (2.8 μs pulse duration); (a) effect of stress on large grain size (200 μm) specimens; (b), (c), and (d) effect of metallurgical condition on spall damage (momentum trap is 99.5% pure copper whereas other copper is 99.9% pure). [From Christy, Pak, and Meyers (1986)].

swaged conditions. Rabin and German (1988) showed that increasing tungsten content in W composites results in strengthening and a drastic decrease in ductility. Bose, Sims, and German (1988) studied the influence of the test temperature and strain rate sensitivity of 90W–7Ni–3Fe alloy and showed that the yield strength increases only slightly with strain rate while the tensile ductility decreases. Meyer et al. (1983) evaluated the dynamic strength and ductility of tungsten alloys in the as-sintered and swaged conditions, showing for each alloy a characteristic increase in strength and a decrease in ductility by increasing the strain rate from 10^{-3} to 5000 s^{-1}. Lankford et al. (1988) proposed a relationship between the strength and the fracture mode of explosively fractured tungsten composite alloys. This relationship indicated a change from cleavage fracture mode in the tungsten particles for

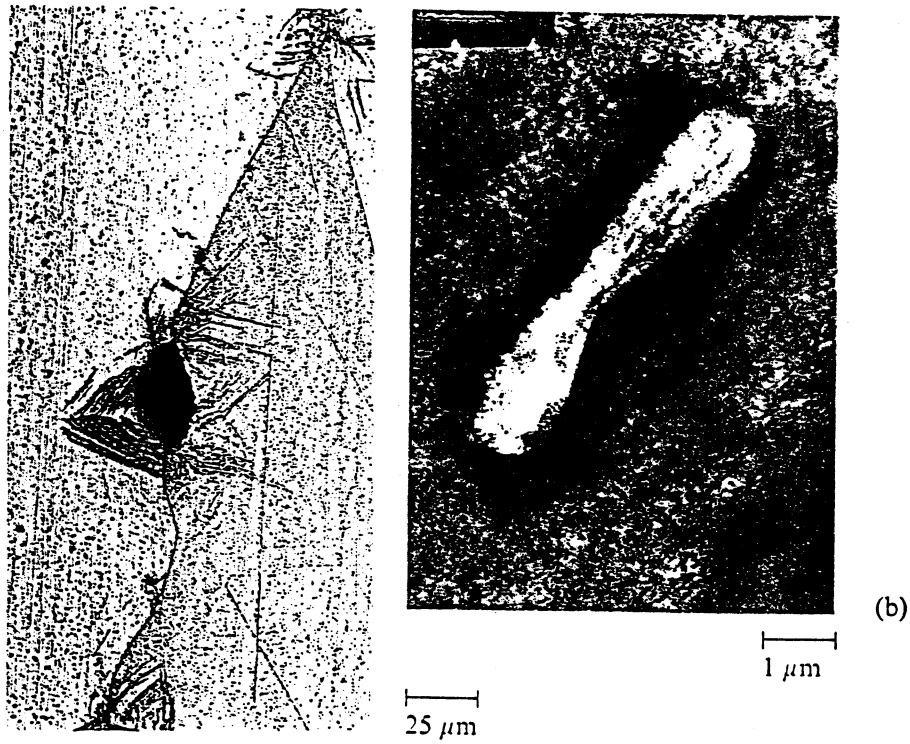

Figure 2.11. (a) Optical micrograph of intergranular void in copper showing markings due to slip. (b) High-voltage transmission electron microscopy of copper void showing plastic deformation region surrounding void; void is peanut-shaped. [From Christy, Pak, and Meyers (1986)].

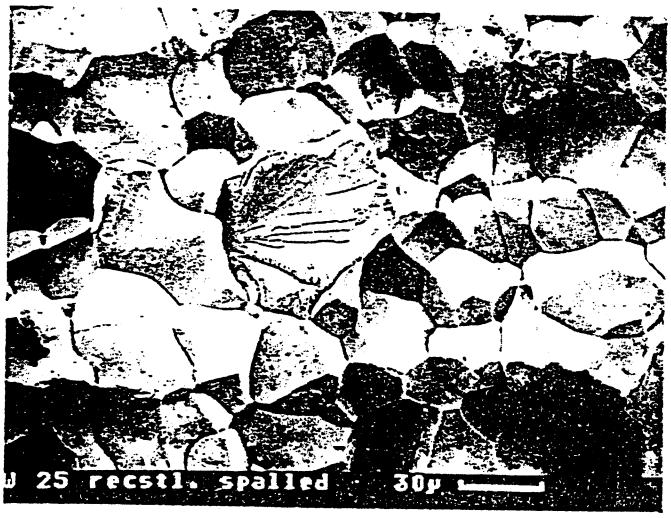

Figure 2.12. Intergranular fracture of spalled surface of recrystallized tungsten. [From Zurek and Gray (1991)].

Figure 2.13. Transgranular fracture of spalled surface of cold-rolled tungsten. [From Zurek and Gray (1991)].

low strength tungsten alloys to an interfacial tungsten–tungsten/tungsten–matrix mode of fracture (a combination of W cleavage and interphase fracture) for high strength tungsten alloys.

In the case of recrystallized W, high strength, low work hardening and high sensitivity to impurities on the grain boundaries of this metal account for its extremely poor ductility. The high resistance to plastic flow in tungsten at ambient temperature results in attainment of flow stress levels above the grain boundary fracture stress. This leads to intergranular fracture before significant plastic flow occurs as shown in Figure 2.12, and virtually zero spall strength of this material [Zurek and Gray (1991)].

Addition of mobile dislocations through cold-working and reduction in interstitial segregation to the grain boundaries improves the spall strength. This is reflected by a change in mode of fracture from intergranular to transgranular cleavage (Figure 2.13).

Alloying of the intrinsically brittle tungsten with a total of 10% Ni and Fe by volume (W–Ni–Fe alloy), improves the spall characteristics even further. The significant increase in spall strength of this alloy (spall strength comparable to the spall strength of copper), is believed to reflect the strong influence of the ductile Ni–Fe matrix and W–matrix interfaces rather than the fracture behavior of the tungsten particles (Figure 2.14). As suggested by Krock and Shepard (1963), the ductility of the W–Ni–Fe alloy may be attributed to the crack-arresting effect of the matrix layer which surrounds each tungsten grain. Although for all practical purposes one would not consider this a ductile fracture, one should look at it in contrast with the inter-

Figure 2.14. Ductile fracture spalled surface of W–Ni–Fe al [From Zurek and Gray (1991)].

granular fracture for the recrystallized tungsten. It should be kept in m that all the ductile Ni–Fe matrix is concentrated at the boundaries betw the individual tungsten grains. What is observed are remnants of a plastic torn ductile ligament at the individual, brittle tungsten grains as obser previously by Lankford (1988). Tungsten grains, fractured transgranula are also occasionally observed.

2.2.5. Dynamic Fracture in Uranium Alloy: Cavitation

Cavitation is an unusual phenomenon in spall processes. This is due to fact that cavitation processes do not occur readily under high hydrost pressures. At the spall plane the hydrostatic stress is a major fraction of spall stress of the material, as shown in Eq. 2.1, Duvall and Fowles (196

$$p = \sigma_{\text{spall}} + 2(1 - 2\nu)/3(1 - \nu)\sigma_{\text{HEL}}, \qquad (2$$

where p is hydrostatic stress, σ_{spall} is a spall strength, σ_{HEL} is Hugoniot ela stress, and ν is the Poisson constant.

The fracture surfaces of U-3/4Ti samples spalled at different applied p sures are shown in Figure 2.15.

The fracture mode is predominantly ductile dimples with many la cracks normal to the spall fracture surface. An optical micrograph of specimen cross section near the fracture surface of the spalled sampl provided in Figure 2.16. It shows major cavitation just below the spall fr ture surface [Zurek (1993)].

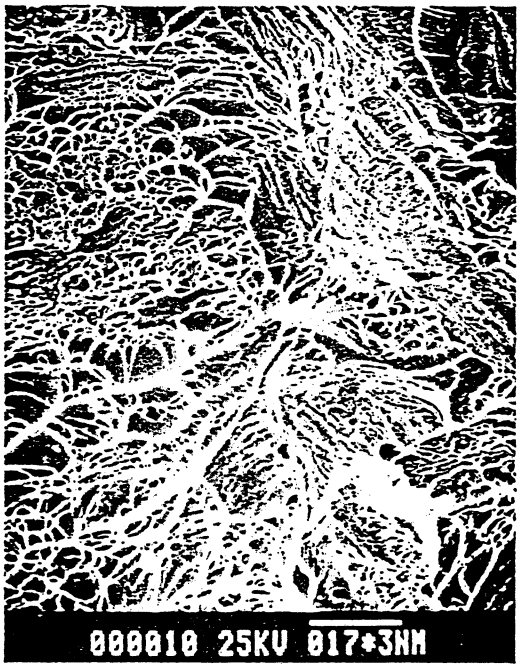

Figure 2.15. Spall fracture surface in U-3/4Ti alloy.

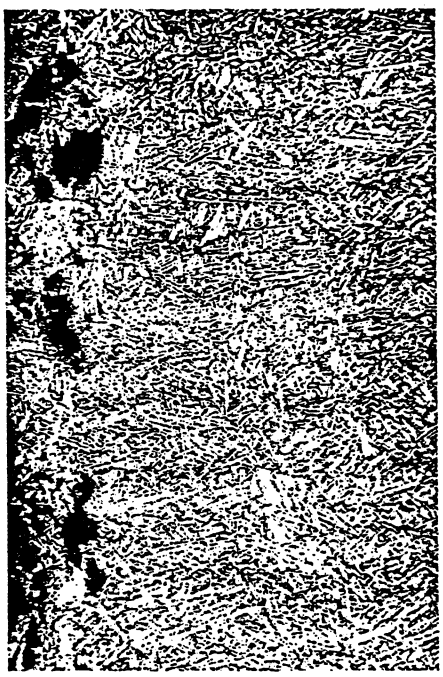

Figure 2.16. Cavitation in subfracture surface of U-3/4Ti alloy.

2.3. Shear Band Instability

2.3.1. General Description of the Phenomenon

Shear bands are macroscopic, non-crystallographic regions where plastic deformation in a material is highly concentrated. The formation of these shear bands is extremely important in dynamic deformation of materials because they are often precursors to fracture.

At low strain rates and moderate levels of strain, slip and twinning are the most common deformation mechanisms in metals and alloys. Both mechanisms are highly correlated with the crystallography of the material. At higher levels of strain and strain rates, deformation instabilities, such as adiabatic shear bands (ASB), may develop. These bands are planar in nature and their formation is related primarily to the specimen geometry, deformation process, and mechanical properties of a material rather than to the local crystallography [Hatherly and Malin (1984)]. Adiabatic shear bands can be formed during compressive or shear loading, and are frequently observed to initiate and propagate cracks or voids followed by fracture and fragmentation of the components. The first reported observation of adiabatic shear bands was made by Zener and Hollomon (1944). They inferred that the observed shear localization was due to the deformation-induced temperature rise at rapid rates of loading. Thermal softening thus overrode strengthening effects due to strain and strain-rate increases.

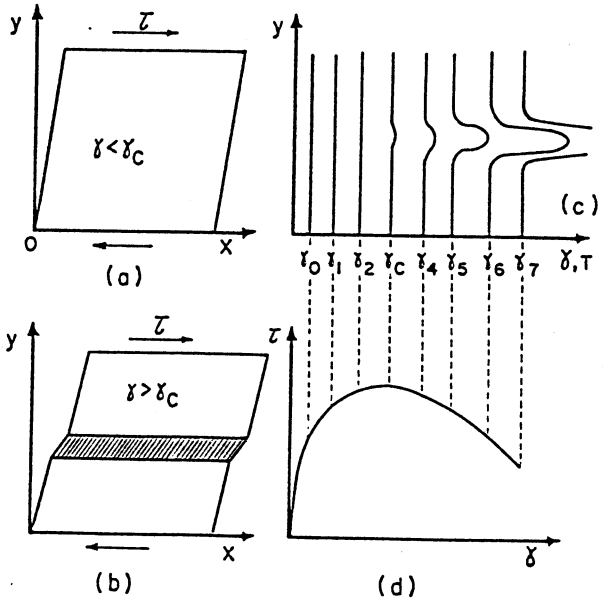

Figure 2.17. Strain evolution and localization beyond γ_c; (a) and (b) homogeneous and localized shear strains; (c) strains and (d) stress–strain curves. [From Meyers (1994)].

The following effects either contribute to or oppose shear-band formation:

opposing factors:	strain hardening and strain-rate hardening
favoring factors:	geometric softening and thermal softening

Figure 2.17 provides a simple explanation for the mechanics of shear band formation. A parallelepiped is being homogeneously sheared by τ (Figure 2.17a). At a certain strain, γ_c, deformation localizes in a band, as shown in Fig. 2.17(b). Figure 2.17(c) shows the progression of strain (or temperature) as a function of the increasing applied stress τ. The strain is homogeneous throughout the specimen at first: $\gamma_0, \gamma_1, \gamma_2$. At γ_c a small fluctuation appears, that accentuates itself as the applied stress is increased: $\gamma_4, \gamma_5, \gamma_6, \gamma_7$. This localization results from softening dominating hardening. A generic stress-strain curve in Figure 2.17(d) shows that softening dominates beyond γ_c, the strain at which the stress is maximum.

The formation of voids and their coalescence into cracks along shear bands is illustrated in Figure 2.18. These voids (marked by arrows) are produced by tension, due to residual stresses or tensile reflections. Since the flow stress of the material within the band is much lower than in the surrounding

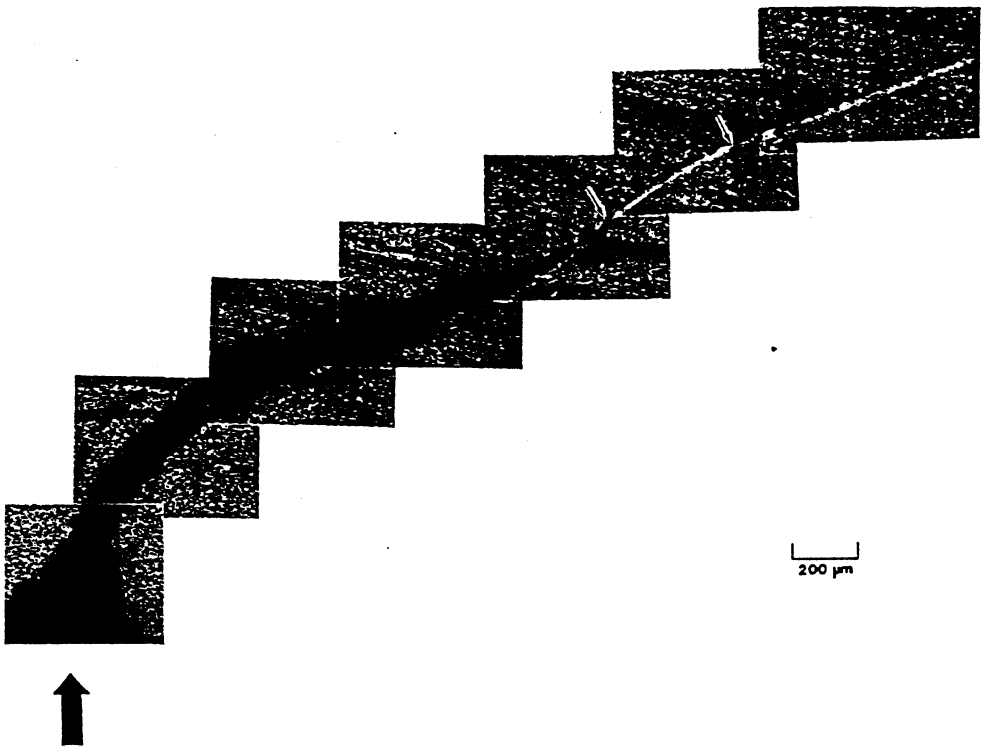

Figure 2.18. Shear-band (top right) and progressive void formation leading to fracture (bottom left) in titanium. [From Grebe et al. (1986)].

material (due to the higher temperature), voids will form there and their diameter is equal to the thickness of the band. When the density of these voids reaches a critical level, they coalesce, forming a crack (lower left-hand side of photomicrograph).

The simplest analytical expression for the formation of a shear band starts with a general constitutive equation represented by:

$$\tau = f(\gamma, \dot{\gamma}, T), \tag{2}$$

where γ, $\dot{\gamma}$, and T are the strain, strain rate, and temperature, respectively. Differentiating:

$$d\tau = \left(\frac{\partial \tau}{\partial \gamma}\right)_{\dot{\gamma},T} d\gamma + \left(\frac{\partial \tau}{\partial \dot{\gamma}}\right)_{\gamma,T} d\dot{\gamma} + \left(\frac{\partial \tau}{\partial T}\right)_{\gamma,\dot{\gamma}} dT \tag{3}$$

$$\frac{d\tau}{d\gamma} = \left(\frac{\partial \tau}{\partial \gamma}\right)_{\dot{\gamma},T} + \left(\frac{\partial \tau}{\partial \dot{\gamma}}\right)_{\gamma,T} \frac{d\dot{\gamma}}{d\gamma} + \left(\frac{\partial \tau}{\partial T}\right)_{\gamma,\dot{\gamma}} \frac{dT}{d\gamma} \tag{4}$$

The condition for instability is:

$$\frac{d\tau}{d\gamma} = 0 \tag{5}$$

If the experiment is conducted at a constant strain rate, $d\dot{\gamma} = 0$, equation 4 is reduced to:

$$\left(\frac{\partial \tau}{\partial \gamma}\right)_{T} = -\left(\frac{\partial \tau}{\partial T}\right)_{\gamma} \left(\frac{dT}{d\gamma}\right) \tag{6}$$

A number of theories for the formation of shear bands have been proposed; current formulations use the perturbation method to predict the onset and propagation of shear bands [(Bai (1981), Clifton (1979), Molinari and Clifton (1983), Grady (1980), Wright (1987)]. A perturbation in the strain or temperature "triggers" the localization of deformation at some plastic strain above the maximum of the τ, γ curve ($d\tau/d\gamma = 0$).

The following materials are known to exhibit shear bands: steels: 1040, 1080, 4340, etc. steels, tungsten heavy metal and alloys (W–Cu–Ni), brass, uranium alloys, zirconium alloys, aged aluminum alloys, titanium and its alloys, shock hardened copper, tungsten-titanium alloy, brasses. Most quenched-and-tempered steels possessing a martensitic microstructure exhibit shear bands. The number of alloys exhibiting shear localization under high-strain-rate deformation greatly exceeds the above list, and virtually any material can exhibit shear-band formation if work hardening is appropriately depressed (e.g., by plastic deformation).

Shear bands do not form simultaneously over the entire surface of a discontinuity, but are better visualized as "initiation" and "propagation" events. The schematic depiction in Figure 2.19 shows the two alternative concepts: the left-hand side shows the simultaneous shearing along a surface (or region of defined thickness), whereas the right-hand side shows the initia-

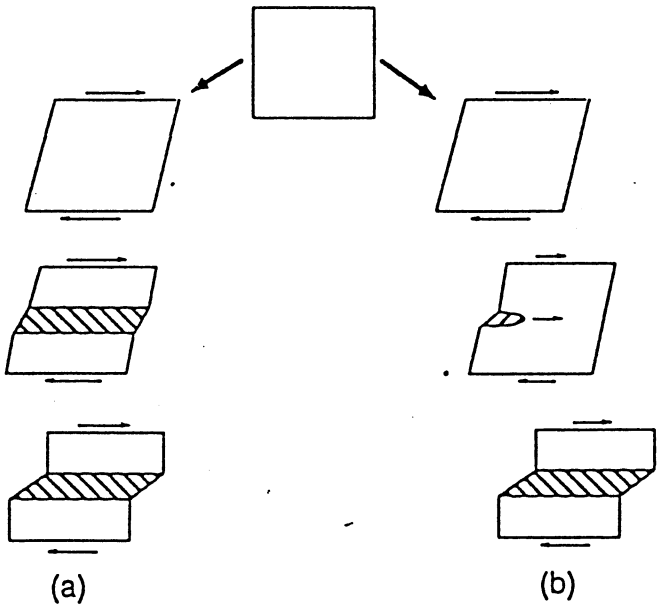

Figure 2.19. Two alternative paths leading to shear-band formation; (a) simultaneous shearing along hatched region; (b) propagation of shear localization by means of advance of shear-band front. [From Meyers (1994)].

tion of a band and its propagation as a shear crack. The latter evolution is thought to represent the actual formation of the shear band. Thus, it is similar to the propagation of a shear crack, leading Grady (1993) to propose a criterion similar to a critical shear-band toughness. Curran and Seaman (1986), Kuriyama and Meyers (1986), and Grady (1993) have modeled the shear band as an advancing region. With this in mind, the initiation of shear-band formation is an important event, and the identification of initiation sites is critical. Figure 2.20 shows a number of possible initiation sites. They have been classified into geometrical and microstructural. External, geometrical sites are easy to envisage, since they are regions where the concentration of strain leads to a temperature rise with thermal softening. The extremities of the softened region are subjected to a stress concentration which, in turn, leads to a stress concentration and the propagation of the band. Internal, microstructural initiation sites operate in the same manner. Several internal sources of strain concentration and/or softening are shown in a schematic fashion. Dislocation pile-ups can, upon their release, pierce through a grain, generating localized heating (Fig. 2.20c). This was initially proposed by Armstrong, Coffey and Elban (1982). If a grain contains a fractured second-phase particle, strain concentration occurs at the extremities of fracture in the matrix, by virtue of sliding of the fractured interfaces (Fig. 2.20d). If a crystal is favorably oriented for rotational softening, its Schmid factor will decrease with plastic strain, decreasing its "effective" flow stress. This leads, in turn, to a concentration of strain in this grain (Figure

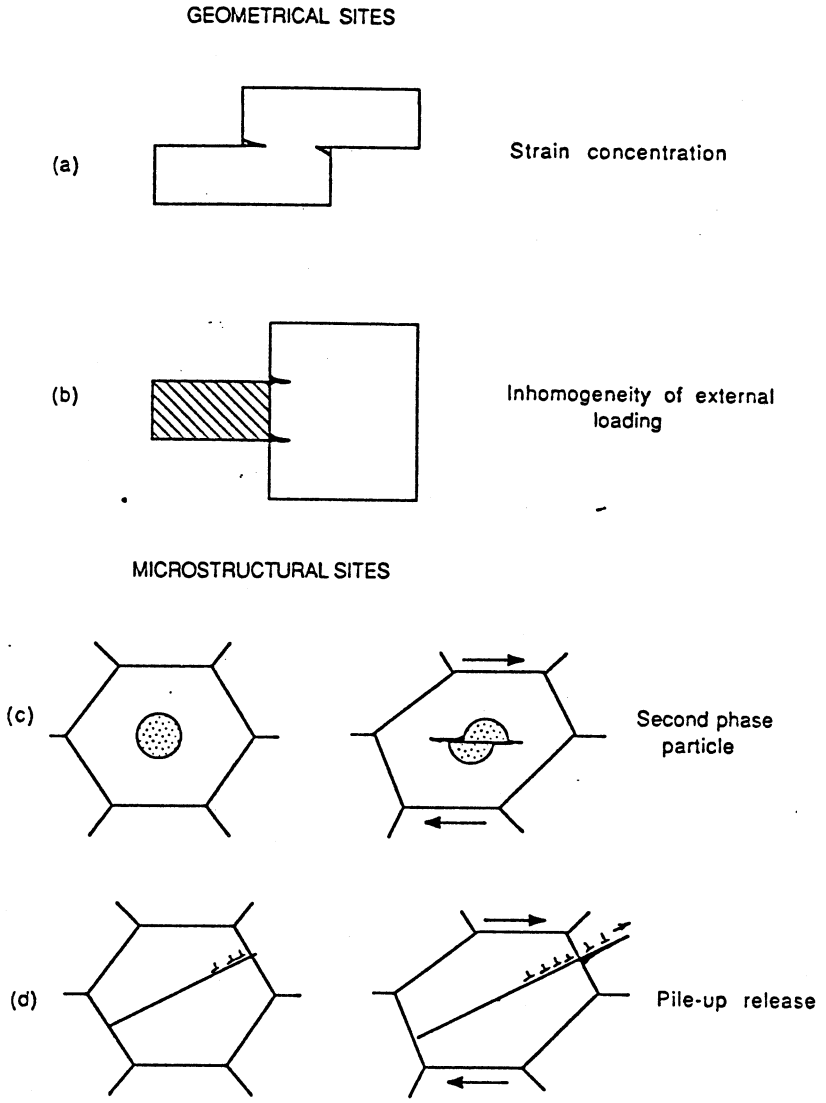

Figure 2.20. Possible initiation sites for shear-band formation; (a), (b) geometrical sites; (c)–(f) microstructural sites. (From Meyers, Subhesh, Kad, and Prasad (1994)).

2.20e). Martensitic lenses or laths are crystallographically oriented within each grain, and interlath or interlens sliding is a favored deformation mechanism because the retained austenite has a lower flow stress than the transformed region. Thus, there will be a tendency for the lenses or laths to orient themselves with the shear direction. This can lead to localized heating, with shear band initiation (Figure 2.20f). A similar situation could arise for deformation twins.

In the subsections that follow we will review the microstructural aspects of shear bands in steels (Section 2.3.2), titanium (Section 2.3.3) and copper (Section 2.3.4).

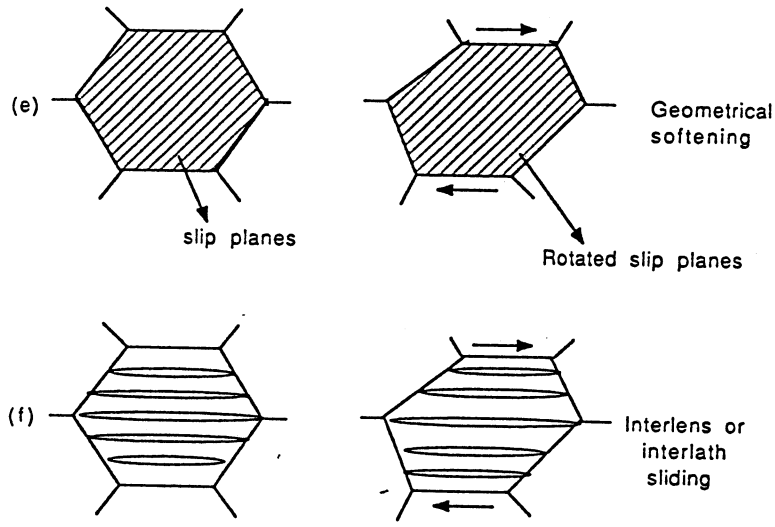

Figure 2.20 (*cont.*)

2.3.2. Shear Bands in Steels

In the case of steels, there is often a "signature" left by the adiabatic shear band in form of a "white etching band" [Rogers (1983)]. Similar etching phenomena were also observed in other materials such as titanium, uranium, etc.. The "white band" is caused by the resolution limit of the optical microscope to resolve the nanometer substructure enhanced by etching. It was believed by early researchers [Hatherly (1984) and Rogers (1983)] that these white etching bands are areas of extremely fine martensite formed during the deformation by locally heating the steel to a temperature above that required for austenitization followed by a rapid quench by the surrounding metal. Definitive proof of this transformation remains to be shown in the literature. Nevertheless, the white etching bands are referred to as "transformed" bands while bands showing high deformation but failing to etch "white" are referred to as deformed shear bands. In addition to the "white" etching signature, these bands are also found to be much harder than the surrounding matrix and are believed to fracture in a brittle manner in steels in the direction normal to the local tensile stress [Rogers (1983)]. Since Zener and Hollomon (1944), there have been numerous works published which have presented experimental observations and models on the subject: Hartley et al. (1987), Asaro and Needleman (1984), Mescall and Rogers (1989), Clifton et al. (1984), Marchand and Duffy (1987), Seaman et al. (1985).

At present, it is generally accepted that adiabatic shear bands occur most readily in materials with a low strain-hardening coefficient, a low strain-rate sensitivity, a low thermal-conductivity and a high thermal softening rate. In addition, shear bands form more readily in high strength materials where the

plastic work due to deformation is greater for a given plastic strain increment [Hartley et al. (1987)].

In recent years several investigations have concentrated on the microstructural study of adiabatic shear bands in steels. Glenn and Leslie (1971) studied shear bands produced in ballistic experiments in low carbon martensitic steels. They identified the structure of white etching bands, using a diffraction method, as very rapidly quenched martensite. Wingrove (1971), using transmission electron microscopy, also identified the adiabatic shear band region as atypical looking martensite, with a high density of dislocations and cells. Thorton and Heiser (1971) studied ASB's in explosively-loaded steel cylinders. The X-ray diffraction pattern of the ASB zone, obtained using chromium radiation in a back reflection Laue method, showed it to be a body-centered-tetragonal martensite. Additional analysis using an electron-beam microprobe showed no chemical segregation associated with the ASB. Derep (1987) studied the microstructural transformation induced by adiabatic shearing in French armor steel. Using electron diffraction in the TEM, he characterized the microstructure observed in the center of an ASB as a fine-grain equiaxed delta ferrite structure, containing very narrow laths of martensite. Wittman et al. (1990) and Meyers and Wittman (1990), have presented a study of microstructural analysis of adiabatic shear bands formed in 4340 quenched and tempered steel [Wittman et al. (1990)] and also in a low carbon steel [Meyers and Wittman (1990)]. They reported that adiabatic shear bands formed in explosively deformed 4340 steel consisted of Fe_5C_2 carbides in a martensitic structure similar to the matrix but that the martensite had lost its original shape. The carbides were observed to have segregated on the internal microtwins. In a low carbon steel [Meyers and Wittman (1990)], the adiabatic shear bands were observed only in the quenched and quenched-and-tempered steel subjected to impact in the velocity range of 450 to 1,050 m/s. It has been hypothesized that the ASB are regions of very fine microstructure with a high concentration of supersaturated carbon which would explain a dramatic hardness rise within the adiabatic shear band [Meyers and Wittman (1990)]. However, no actual chemical analysis of the shear band was obtained in this study.

Most recently, a dynamic punch-impact test was designed by Zurek (1993) to produce white-etching adiabatic shear bands in pearlitic and martensitic 4340 steels. The average strain of 0.5 and the associated average strain rate of 18000 s^{-1} were sufficient to induce an adiabatic shear band instability in these steels. Figures 2.21 and 2.22 show results obtained for the martensitic quenched and tempered 4340 steel. The lath structure characteristic of quenching is prominent in the matrix; the corresponding diffraction pattern is also shown. Within the shear band (Figure 2.22) the microstructure is quite different, with small features that could be microcrystals.

These features have sizes between 10 and 30 nm, consistent with the observations of Meunier et al. (1992) and Beatty et al. (1992). Meunier et al. (1992) identified the structure of shear bands produced by ballistic impact

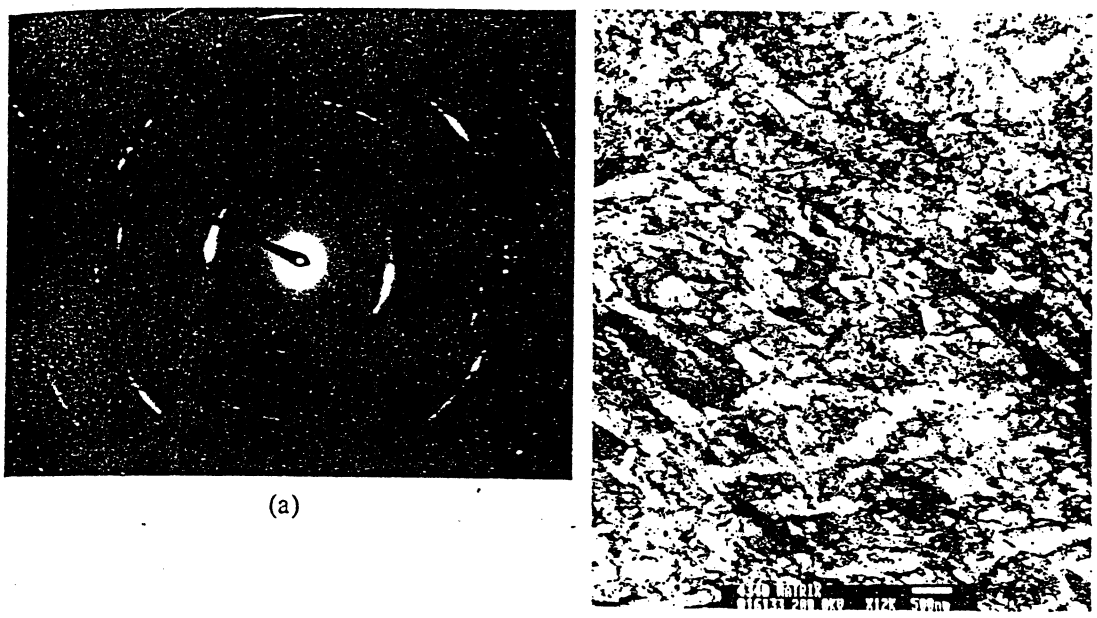

(a)

(b)

Figure 2.21. TEM of 4340 quenched and tempered martensitic matrix and diffraction pattern.

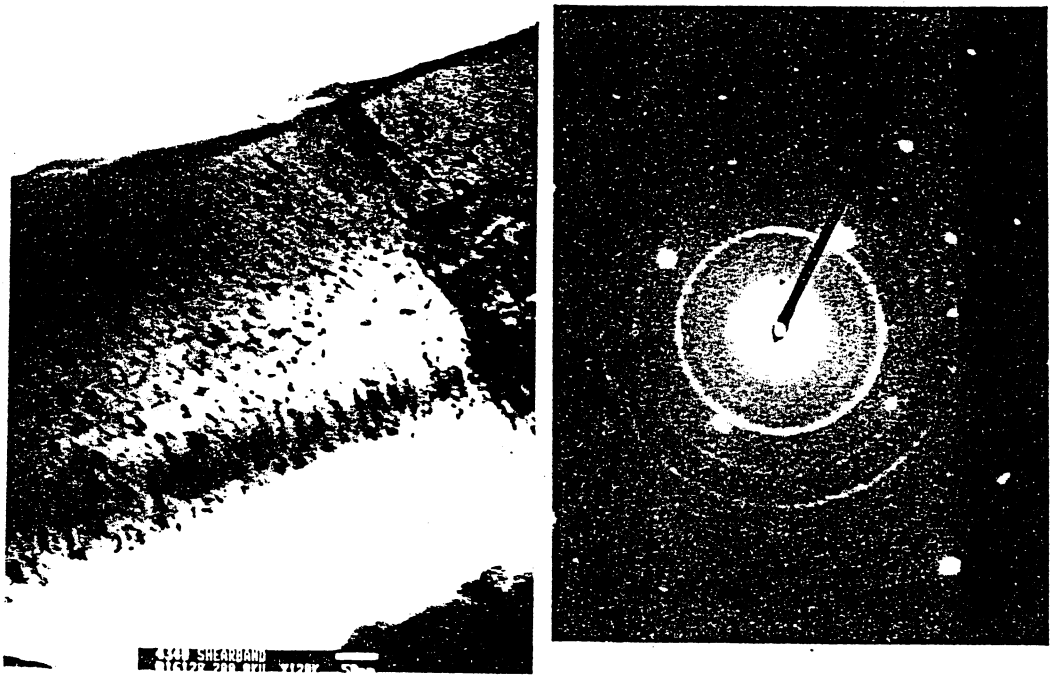

Figure 2.22. TEM of 4340 quenched-and-tempered martensitic shear band and diffraction pattern.

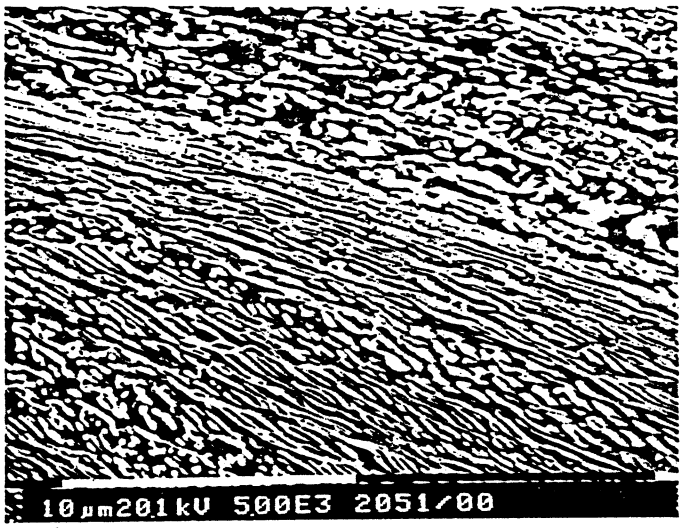

Figure 2.23. Partially spheroidized microstructure inside a shear band in pearlitic 4340 steel. [From Zurek (1993). Submitted for publication.]

and found it consisted of small (< 50 nm) grains; carbides were dissolved. Beatty et al. (1992) conducted similar observations on a quenched-and-tempered martensitic 4340 steel. They found grain sizes varying between 8 and 20 nm inside of the shear band.

In pearlitic steels, the microstructural evolution is quite different. Figure 2.23 shows the partial spheroidization of the cementite within the adiabatic shear band. This suggests a local temperature increase above 650°C and an extremely rapid spheroidization. A local shear strain within the shear band of $\gamma = 4$–5 caused the Fe_3C to deform and fragment and at the same time accelerated the kinetics of spheroidization. Uvira et al. (1972), Robbins et al. (1964), Chojnowski and Tegart (1968), Hirano (1963), and Zurek (1993) suggested that during high temperature deformation the lamellar carbides would spheroidize due to both fracture of the carbide plates and to "short-circuiting" carbon and iron diffusion paths associated with the creation of very fine ferrite subgrains. Nanohardness differences found across the adiabatic shear band compared to the deformed and undeformed regions were thought to be due to the refinement, deformation and partial spheroidization of the microstructure, rather than phase transformation or carbon segregation within the adiabatic shear band. Zurek (1993) found no chemical segregation in the region of the adiabatic shear band with respect to the matrix material.

In a shear band, large shear leads to fragmentation and work hardening but the rate of damage accumulation which causes fracture must depend on the level of tensile stress across the band. This supports the observation that ductile fracture was the primary mode of failure at the termination of the

shear bands. Finally, the "white" etching bands in steels are beyond the optical microscope resolution limit and are not necessarily an indication of phase transformation.

2.3.3. Shear Bands in Titanium and Titanium Alloys

Titanium shows a great propensity for shear-band formation because of its strain rate sensitivity, low thermal conductivity, and low heat capacity. Grebe, Pak and Meyers (1985), Meyers and Pak (1986), and Meyers et al. (1993), investigated the microstructure of shear bands in titanium and Ti-6Al-4V alloy. Two methods were used for the generation of shear bands: (a)

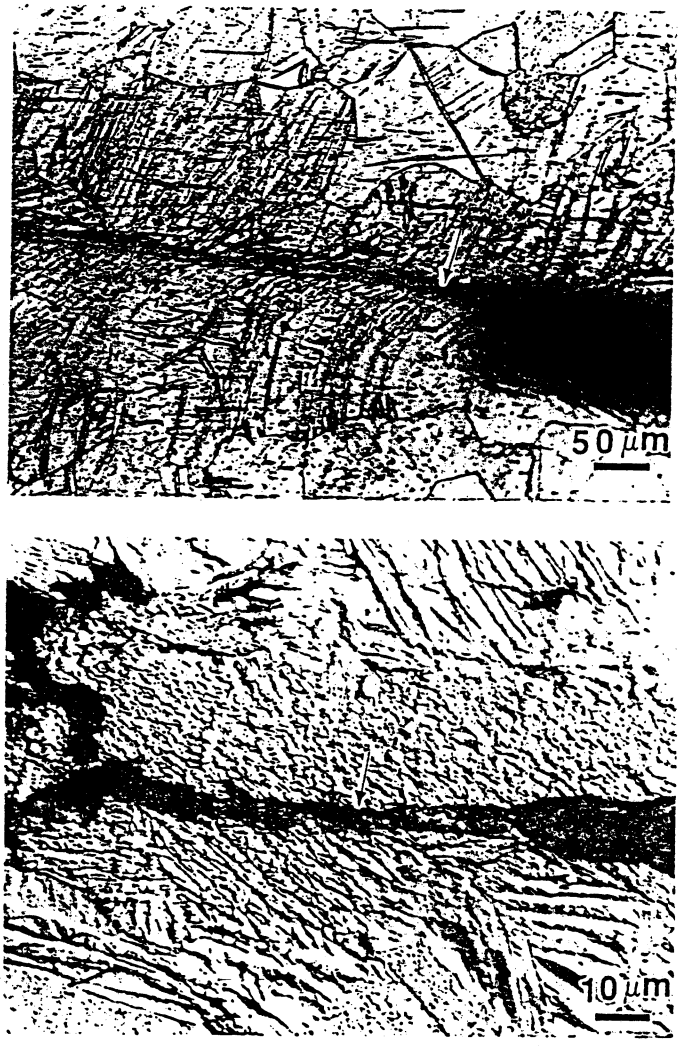

(a)

(b)

Figure 2.24. Cracks (a) initiated; and (b) propagated along shear band in titanium [From Meyers et al. (1993)].

(a)

(b)

Figure 2.25. Transmission electron micrograph of shear band in titanium. (a) Shear band generated by ballistic impact. [From Grebe et al. (1986).] (b) Shear band generated in Hopkinson bar. [From Meyers et al. (1994).] (c) Diffraction pattern showing microcrystalline structure.

impact at 600 m/s of a cylindrical projectile on a titanium plate; and (b) rapid shearing of a narrow band produced in a hat-shaped specimen placed in a compression Hopkinson bar. These two widely different techniques produced shear bands that were essentially identical. These shear bands varied in width from 2 to 20 μm; their width was found to increase with shear strain. They formed at a critical shear strain of 1.5. These shear bands were inevitably precursors to failure, as shown by the cracks propagating along the shear-band path, Figure 2.24.

(c)

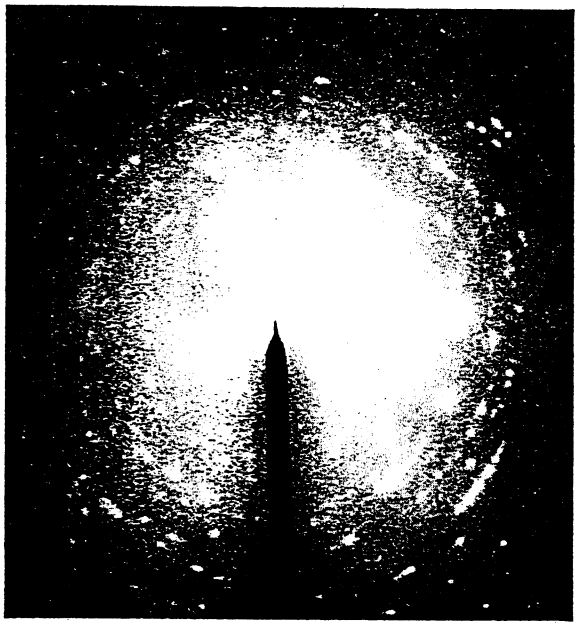

Figure 2.25 (*cont.*)

Figure 2.24(a) shows the onset of fracture, whereas Fig. 2.24(b) shows a fully formed crack. The crack initiated at an external strain concentration (see Figure 2.20(a)). Transmission electron microscopy conducted by Meyers and Pak (1986) revealed that the shear-band interior consisted of very small grains, 0.05 to 0.3 μm in diameter, with a low dislocation density (Figure 2.25(a)). Pak et al. (1986) suggested that this microstructure was formed by a dynamic recrystallization process. The results obtained by Meyers et al. (1994) on shear bands produced under prescribed conditions of strain and strain rate are essentially the same as the earlier study of Meyers and Pak (1986) and Grebe et al. (1983). The shear-band microstructure, produced in Hopkinson bar experiments by Meyers et al. (1994) also consisted of the small grains with a very low dislocation density shown in Figure 2.25(b). The grain boundaries between these grains are well defined and the microstructure between adjacent grains varies between low-angle and high-angle boundaries. The diffraction pattern of Fig. 2.25(c) illustrates the microcrystalline nature of the structure as well as the wide variety of misorientations between micrograins.

2.3.4. Shear Bands in Copper

While annealed copper does not show localization of plastic flow under normal loading situations, the passage of a shock wave can significantly increase the flow stress, and reduce the work hardening rate, rendering it

Figure 2.26. Transmission electron micrograph and diffraction pattern of shear band in pre-hardened copper. (From Meyers et al. (1991).]

susceptible to localization. Indeed, Tang et al. (1991) found shear localization regions in recovered explosively forged copper projectiles.

Meyers et al. (1992) and Andrade et al. (1994) subjected copper to shock pre-conditioning at 50 GPa and subsequently studied its response under high strain, high-strain-rate loading. The microstructure within the shear bands (produced in a hat-shaped specimen, using a Hopkinson pressure bar) resembled the ones observed in steel (Section 2.3.2) and titanium (Section 2.3.3). After a critical shear strain $\gamma \sim 2$, the specimen formed a well defined shear band, of a width of $\sim 200\ \mu$m. Figure 2.26 shows a transmission electron micrograph of the shear band and the associated diffraction pattern. The microcrystalline structure within the band is readily evident. Small, equiaxed grains with a low dislocation density are present. The diffraction pattern, consisting of almost continuous rings, shows that the micrograins have a wide range of orientation. This microcrystalline structure is indicative of a dynamically recrystallized structure.

2.4. Stress Wave Effects in Rocks and Ceramics

A shock wave propagating in rocks and ceramics leads to fragmentation rather than shock strengthening. A tensile release wave activates the flaws generated under compression and produces spalling at a low stress level. Models describing the propagation of high amplitude disturbances in rocks and ceramics should incorporate the time dependency of the fragmentation process. Experiments by Aimone, Meyers, and Mojtabai (1984) on a quartz monzonite rock subjected to a uniaxial strain plane compression pulse showed that:

a. The mean fragment size decreases with increasing pulse duration at constant pressure, and with increasing pressure at constant pulse duration. This is shown in Figure 2.27(a) for quartz monzonite copper porphyry subjected to different shock-wave pulses.

b. The internal damage generated in rocks by passage of a shock wave is much larger than the damage simply observed by the fragments. The total surface area of cracks generated internally is higher, by at least one order of magnitude, than the surface area of the observed fragments. This can be verified by converting the internal damage into an "equivalent fragment size." This was accomplished by using the expression $D = 6/S_v$ defined earlier. Figure 2.27(b) shows the measured surface area per unit area (total area of cracks). The "equivalent" particle size is shown in Fig. 2.27(c). The differences in particle size between Figs. 2.27(a) and (c) are of the order of magnitude 10^2. Thus, a great portion of the damage remains hidden inside the fragments.

The time dependent failure of rocks is consistent with the concepts of nucleation, growth, and coalescence. If a description of how a shock wave propagates through a rock is attempted, it has to incorporate these effects. The energy dissipated by the wave in the fragmenting rock or ceramic is associated with the following energy storage mechanisms: generation of cracks, possible phase transformation, twinning, interfacial defects, sliding of the crack surfaces, porosity collapse, and dislocation motion; of these, the energy expenditure associated with pore collapse is the highest dissipative component in rocks.

Spall experiments conducted by Louro and Meyers (1989) on alumina demonstrated that the extent of damage, measured by S_v, the surface area of cracks per unit volume, increased with increasing pulse duration. The results are shown in Figure 2.28(a) and (b).

In Figure 2.28(a) the pressure was varied at a constant pulse duration, for two aluminas: AD 85, and high-purity alumina. The damage in AD 85, an alumina containing considerable porosity and up to 12% of SiO_2, is higher than the high-purity alumina, showing that porosity and grain-boundary phases are a source of damage. The effect of varying the duration of the stress pulse, at a constant stress level, is shown in Figure 2.28(b). The tensile pulse is created by using a capsule with a shock impedance lower than the

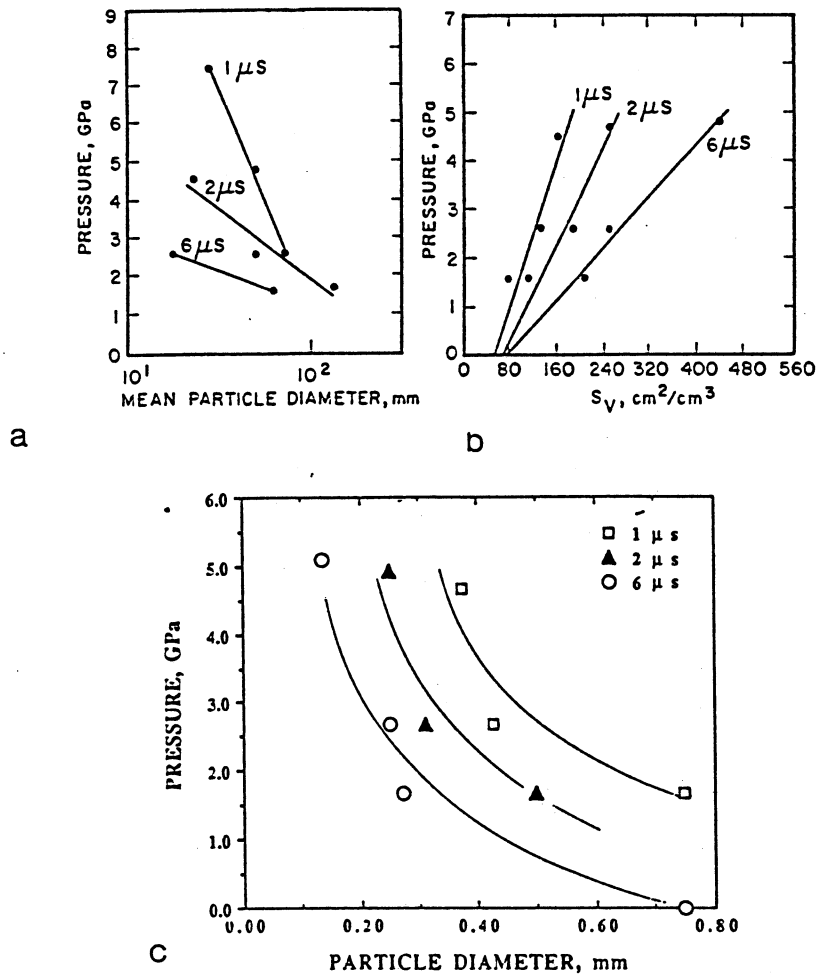

Figure 2.27. Damage in quartz monzonite rock subjected to compressive stress pulses of varying amplitudes and durations; (a) fragment size distribution; (b) and (c) internal damage, expressed as surface area-per unit volume (b) and "effective" particle diameter. [From Aimone et al. (1984).]

alumina, (aluminum). The tensile pulse duration was varied from 0.2 to 1.6 μs, after a constant compressive stress pulse of 4.5 GPa, providing a tensile amplitude of 3.2 GPa.

An important observation made by Louro and Meyers (1989) is that the compressive stress pulse preceding tensile reflection is extremely effective in pre-conditioning the ceramic, by creating cracks that are subsequently activated by tension. Thus, two ceramics subjected to identical tensile pulses can exhibit highly different damage levels. The datum point marked ◩ in Figure 2.29 illustrates this well. Aluminum and epoxy were used as backing materials. Epoxy has a very low shock impedance and the tensile pulse generated, for a specific compression pulse, is much higher than with aluminum backing. For a 4.6 GPa compressive pulse, the tensile pulse has an amplitude of 4.3 GPa. Figure 2.29 shows that the large tensile stress did not cause a signif-

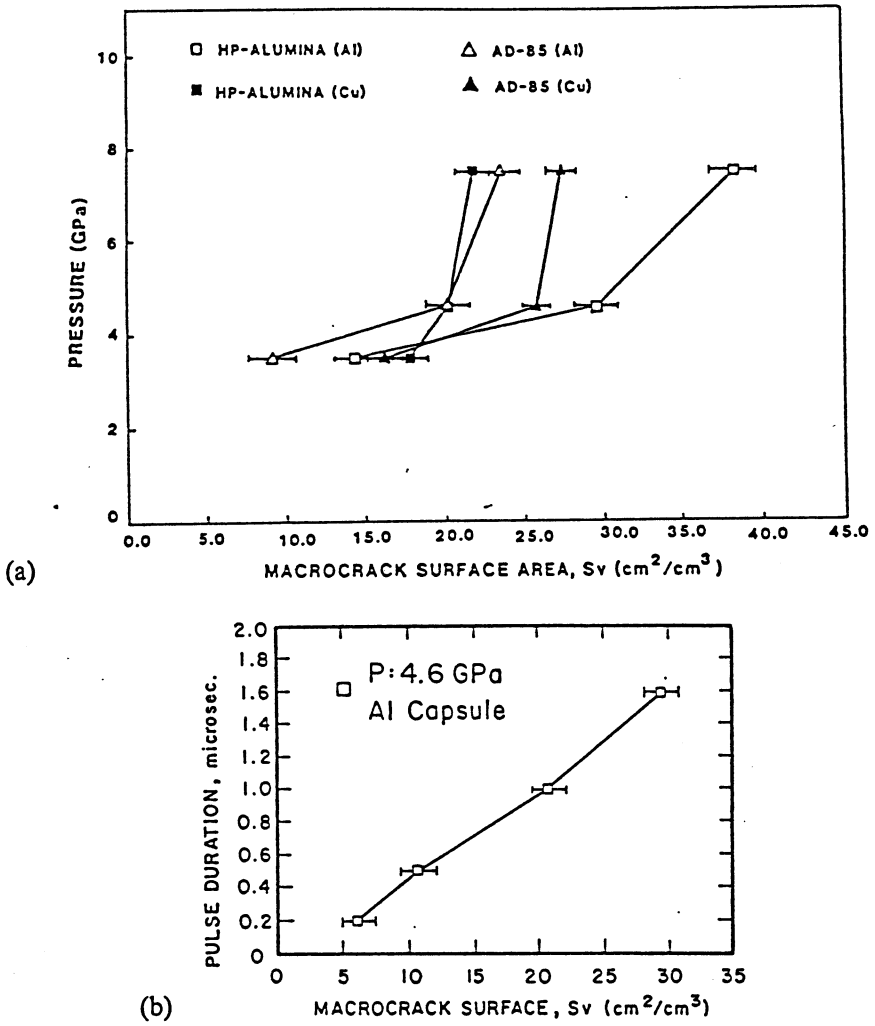

Figure 2.28. Effect of (a) pressure and (b) pulse duration on the damage produced in alumina. (From Louro and Meyers (1989).]

icant increase in fragmentation. The epoxy-backed alumina (which exhibited a tensile pulse close to the compressive pulse and is marked ◩) is the isolated point in Figure 2.29. All other data points (falling on roughly the same line) correspond to tensile stresses preceded by compressive stresses three times higher in amplitude. The latter pulses were produced in alumina capsules (where the tensile pulse amplitude is ~30% of the compressive pulse). If exposure to compression prior to tension did not have an effect on fragmentation, the point marked ◩ should fall on the same line as the other points, and S_v should be approximately 80 cm^2/cm^3, instead 32 cm^2/cm^3. This result emphasizes the important role played by prior compressive pulse in determining the alumina fragmentation. The effect of grain size on damage was also investigated by Louro and Meyers (1989). The results are shown in Figure 2.30, where two grain sizes, 4 and 24 μm, of the same material, are shown.

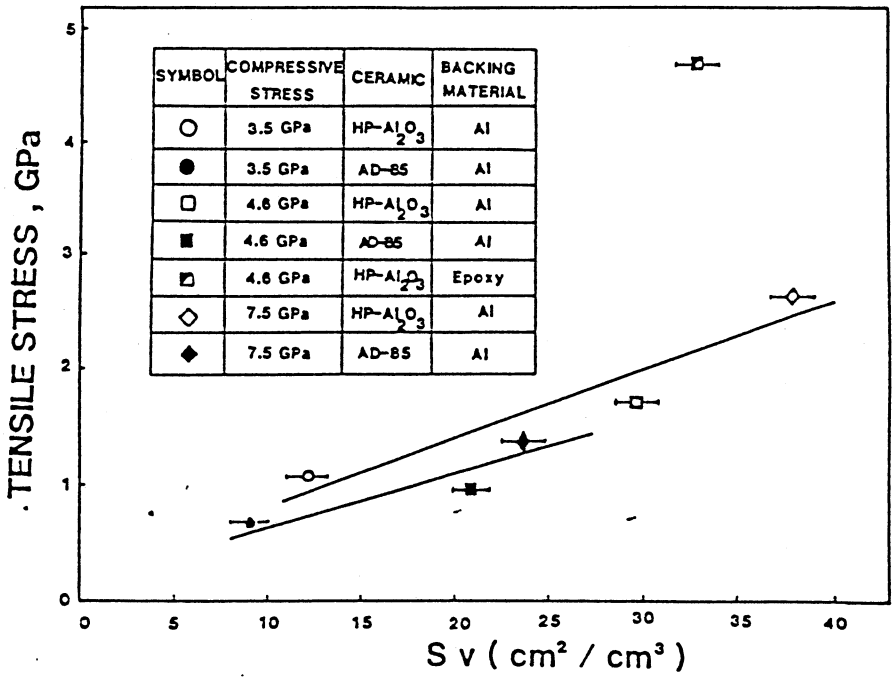

Figure 2.29. Effect of tensile stress amplitude on damage in alumina; notice point ◩ which corresponds to a lower compressive pulse amplitude. [From Louro and Meyers (1988).]

The smaller grain size exhibits greater damage, under the same loading conditions. The explanation for this behavior is that the density of crack nucleation sites is greater for the smaller grain size. The most obvious nucleation sites for flaws are pores and grain boundaries. The mechanisms by which these compressive stresses can generate flaws are shown, in schematic fashion, in Figure 2.31.

The most important mechanisms are:

a. Spherical voids subjected to compression generate tensile stresses. In Figure 2.31(a) we have σ_θ tensile stress. Therefore, cracks are generated. These cracks are parallel to the direction of load application. This problem was first solved by Goodier (1933).

b. For ellipsoidal flaws, the same phenomenon occurs. Indeed, the spherical case (a) is a special case of the elliptical flaw. Brace and Bombolakis (1963) and Horii and Nemat-Nasser (1986) studied the stresses generated by this configuration. The shear stress due to the applied compressive load, τ, generates tensile stresses at the extremities of the elliptical flaw, eventually cracking them [Figure 2.31(b)].

c. Elastic anisotropy of a polycrystalline ceramic aggregate leads to incompatibility stresses at the boundaries. Figure 2.31(c) shows the "softer" and "stiffer" directions of grains marked by a short ⟩—⟨ and long ⟩——⟨ line respectively. Plastic deformation can occur under compressive loading. When the stress is released, i.e., after the passage of the stress pulse, localized

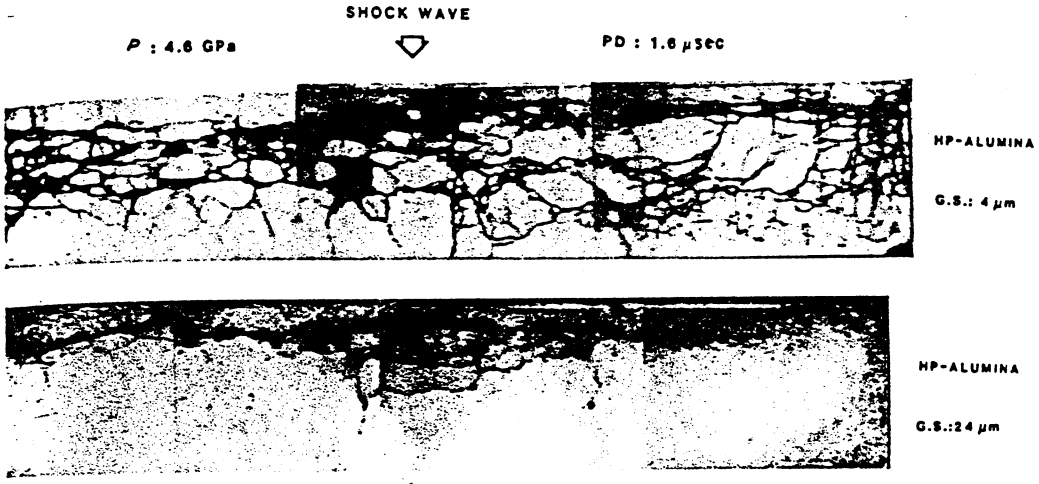

Figure 2.30. Cross-section of alumina disks subjected to compressive stress pulse of amplitude 4.6 GPa and duration 1.6 μs; (a) 4 μm grain size; (b) 24 μm grain size. [From Louro and Meyers (1989).]

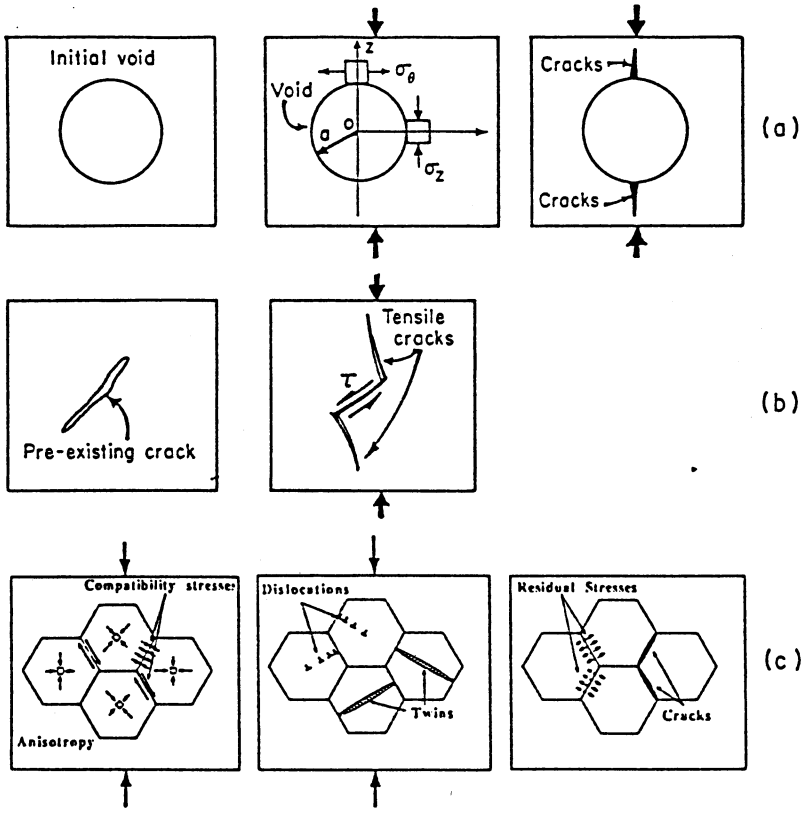

Figure 2.31. Schematic representation of different mechanisms of crack nucleation in ceramics subjected to compressive stress pulses; (a) nucleation at spherical void; (b) nucleation at elliptical flaw; (c) nucleation due to elastic anisotropy of grains. [From Meyers (1994).]

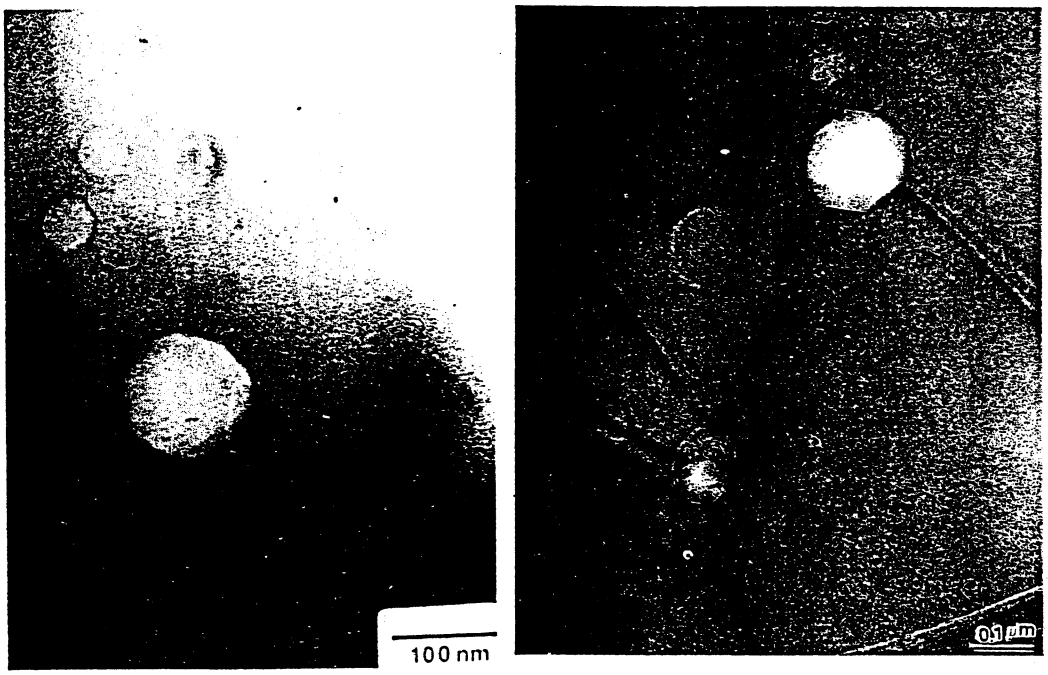

(a) (b)

Figure 2.32. (a) Voids in alumina; (b) cracking at voids after passage of stress wave. [From Louro and Meyers (1989).]

tension regions are created by the residual stresses due to plastic deformation. This can open up cracks. These are not strictly compression cracks but rather "post-compression cracks." Lankford (1977) describes some of these concepts.

Transmission electron microscopy observations can reveal the onset of damage in ceramics subjected to compressive and tensile pulses. Voids in alumina, prior to stress-wave loading, are shown in Figure 2.32(a). The activation of cracks at existing voids is shown in Figure 2.32(b). Cracks, emanating from these voids, are seen very clearly. These cracks have only grown a few micrometers. These cracks can be generated by the mechanism shown in Figure 2.31(a).

Subsequent tensile loading will activate these cracks, if the stress intensity factor and time are sufficient. In Figure 2.33(a), dislocations generated by stress-wave loading (below the material HEL), are shown. The incompatibility stresses can be responsible for the generation of dislocations at the grain boundaries. Alumina, having a hexagonal structure, exhibits an anisotropy of elastic properties. Therefore, stresses build up at the grain-boundary regions, leading to cracks, when unloading occurs. Grain-boundary cracking is shown in Figure 2.33(b). The cracked boundaries are marked by arrows.

The micrographs (TEM) of Figures 2.32 and 2.33 illustrate some of the damage mechanisms in ceramics. In actual ceramics, the presence of grain-boundary phases, of a glassy nature, is often observed. These grain-

Figure 2.33. (a) Dislocations in alumina after passage of stress waves, (b) cracks m alumina (marked by arrows). [From Louro and Meyers (1989).]

boundary phases are the result of additives that are part of commercial ceramics to help the sintering process. These glassy phases have a different shock impedance than the surrounding grains and contribute to failure. The process of fragmentation of ceramics under compressive/tensile pulses will not be discussed here. Figure 2.34 shows, in a simplified manner, how pre-existing flaws (a) can generate cracks; (b), under compression; and how these cracks can grow under tension; (c) fragmenting the ceramic (d). A more detailed treatment with quantitative predictions of fragment size is given by Louro and Meyers (1990). Since this is a dynamic process, the stresses in the regions surrounding cracks are reduced by the free surface generated, and therefore nucleation of cracks in these regions is hampered leading to a fragment size that is a function of both stress amplitude and duration. In Figure 2.34, it is clear that the evolution of damage is determined by the existing flaws or microstructural inhomogeneities in material. These microstructural effects together with the stress history parameters determine the final fragment sizes and size distribution.

It has been conclusively shown by Nesterenko, Meyers, and Chen (1995) that the fragmented (or "comminuted") ceramic will flow by shear localization. This is extremely important for the defeat of ceramic armor, since the ceramic fragmented by the shock wave has to be ejected, for penetration to proceed. Experiments conducted on both granular and fragmented alumina revealed that the plastic deformation proceeds primarily by shear localization, beyond a compressive strain of -0.2. Figure 2.35 shows a section of an

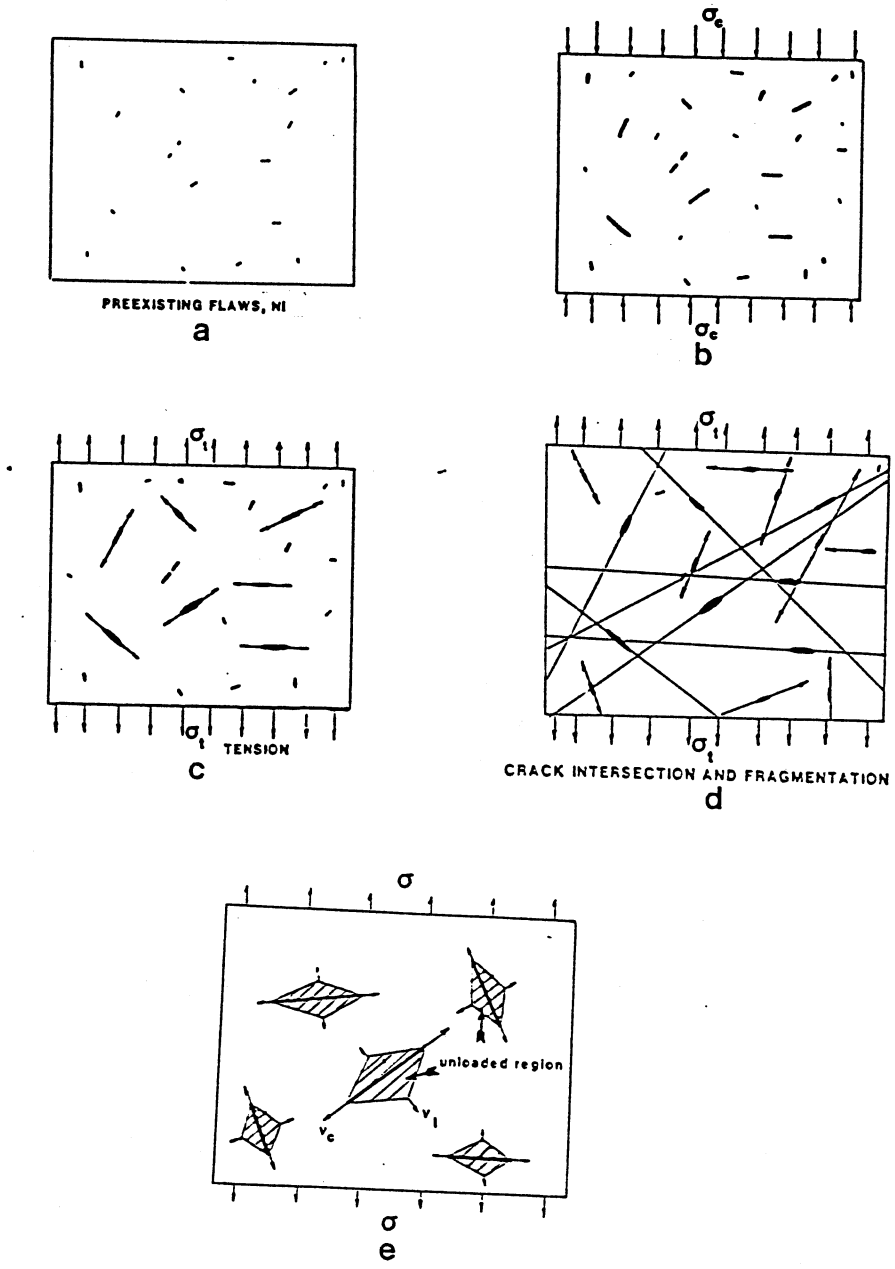

Figure 2.34. Schematic representation of sequence of events leading to fragmentation of brittle material after compression-tension pulse. (a) Initial pre-existing flaws (voids, grain boundary phases, etc.); (b) activation of flaws and formation of cracks by compression; (c) growth of cracks by tension and nucleation of new cracks; (d) intersection of cracks and fragmentation; (e) development of unloaded regions around growing cracks in which no further crack nucleation and growth occurs. [From Louro and Meyers (1990).]

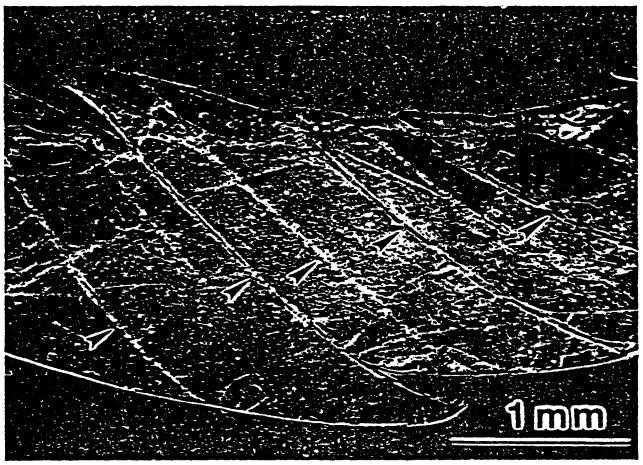

Figure 2.35. Shear localization when densified granular alumina (85% T.D.) is subjected to a compressive tangential strain of ~ -0.3 [From Nesterenko, Meyers, and Chen (1995)].

annular specimen of densified granular alumina after a compressive tangential strain of ~ -0.3. The shear bands are clearly seen (arrows) and have a width of $\sim 10\ \mu m$.

2.5. Summary and Conclusions

The observations reported in this article as well as extensive information in the literature indicate that microstructural aspects are of utmost importance in the dynamic failure of materials.

Dynamic failure was divided into three classes:

1. Dynamic failure by tension; spalling (uniaxial strain state) and uniaxial stress state.
2. Dynamic failure by shear; shear instability is the precursor to this failure mode.
3. Dynamic failure by compression; ceramics, rocks and brittle metals (cast iron, intermetallic compounds) are especially prone to failure under compressive loading.

We summarize below the most important microstructural effects for these three classes of failure.

All microstructural variables play a role in the dynamic failure of materials. The most important variables are:

- grain size
- presence, density, morphology, and size and distribution of second-phase particles
- texture (not mentioned in this chapter)

- impurity atoms and their distribution (e.g., segregation at grain boundaries)
- crystallographic structure (which can be changed by heat treatment, e.g., quenching of steel)
- pre-strain (e.g., annealed vs. shock-hardened material)
- intergranular phases (e.g., glassy phase at grain boundaries of ceramic)
- voids (e.g., porosity in ceramics).

2.5.1. Dynamic Failure by Tension

This failure is determined by the nucleation, growth and coalescence of voids (for ductile failure) or cracks (for brittle failure). The nucleation and growth of different flaws occur independently, in contrast to quasi-static failure, because the rate at which these events occur is such that the stress waves cannot communicate the information to adjoining flaws.

In steels, the transition from ductile to brittle failure is facilitated by a strain-rate increase, because of the strain-rate dependence of the flow stress. The spall failure above 13 GPa has a totally different morphology from the one below 13 GPa, because of the pressure-induced phase transformation.

For copper, grain boundaries and second-phase particles (inclusions) are seen to play a major role in determining the spall strength and fracture morphology. For large-grain-sized specimens, void nucleation takes place at the grain boundaries; although the reasons are not totally understood, grain boundary segregation of impurities (more extensive in large-grain-size specimens, which have a smaller grain boundary area per unit volume) is thought to be the cause. The ratio between nucleation and growth rate determines the size of the dimples and the evolution of damage.

2.5.2. Dynamic Failure by Shear

The occurrence of adiabatic shear bands is determined by the thermomechanical response of the material. The propagation of a shear band occurs by the advance of a shear band tip and the creation, behind it, of a thin region (a few μm) of heated and softened material. This material has a much lower tensile strength than the surrounding matrix, and low tensile stress will induce separation along this region. Upon cooling, the material inside the band often becomes harder and more brittle than the matrix. Therefore, it becomes a favored path for failure; the shear bands can "trigger" both ductile and brittle failure.

All metallurgical parameters which affect the thermomechanical response (and especially, the work hardening, thermal softening, and flow stress) of the material influence its propensity to undergo shear instabilities. These shear bands are the primary path for shear failure. For instance, annealed copper does not undergo shear instabilities under normal loading conditions, whereas it is prone to shear localization after a sufficient hardening. In a similar fashion, pure aluminum does not localize, while aged aluminum

forms shear bands. Pearlitic steel localizes, but with much less intensity than quenched-and-tempered steel.

The evolution of the microstructure within the shear bands is determined by the combination of initial microstructure, plastic deformation and heating and may lead, under certain conditions, to dynamic recovery and/or recrystallization; the microcrystalline structures observed in recovered specimens of titanium and copper are supportive of such mechanisms. Ceramics fragmented by compressive and tensile dynamic loading also deform by shear localization; the softening in this case is not, however, a primarily thermal process.

2.5.3. Dynamic Failure by Compression

Whereas ductile metals can undergo large compressive stresses without failure; in brittle materials (ceramics, rocks, intermetallic compounds, and brittle metals such as cast iron) flaws are generated under compressive stresses. It should be clarified that by virtue of microstructural inhomogeneities, the remote compressive loading causes localized regions of tension which on their turn, lead to crack initiation. Thus, microstructural effects are responsible for cracking under compression. Examples of microstructural inhomogeneities that can nucleate cracks under compression are:

- Voids, around which tensile stresses are generated by compression. These voids can have all kinds of shapes, but spheres and ellipsoids are idealized configurations which lend themselves to mathematical analyses predicting localized regions of tension.
- Grain boundaries between grains in materials having elastic anisotropy in such a manner that elastic incompatibility stresses are generated.
- Brittle grain-boundary phases which may fracture under shear resulting from compression. An example is the glassy grain-boundary phase in commercial alumina. Ceramics often contain these phases, which are due to the sintering agents that are added to material to facilitate densification during processing.
- Second phase particles which may have different compressibilities than the matrix, leading to crack nucleation at the interface.
- Destruction of coherency between the matrix and second phases due to differences of elastic properties.

2.6. Acknowledgments

The writing of this chapter was supported by the Joint DOE/DOD Munitions Technology Program (AKZ) and the U.S. Army Research Office University Research Initiative Program (MAM). The research described was supported by the Joint DOE/DOD Munitions Technology Program and by the Eglin Air Force Base (AKZ) and by the U.S. Army Research Office,

National Science Foundation, and the Center for Explosive Technology Research, New Mexico Tech. (MAM).

Anna K. Zurek would like to acknowledge help and collaboration from G.T. Gray III, W. Blumenthal, T. Lowe, W.J. Wright, T. Zocco, C. Trujillo, and M. Lopez. Marc André Meyers would like to acknowledge help and collaboration from S. Christy, A. Grebe, H-r. Pak, J. Isaacs, K.S. Vecchio, B. Kad, U. Andrade, C.T. Aimone, J.C. La Salvia, H.C. Chen, and Y.J. Chen.

2.7. References

Aimone, C.T., Meyers, M.A., and Mojtabai, N. In *Rock Mechanics in Productivity and Design*, (eds. C.H. Darding and M.M. Singh), SME-AIME, 979 (1984).

Andrade, U., Meyers, M.A., Vecchio, K.S., and Chokshi, A.H. *Acta Met. and Mat.*, 42, 3183 (1994).

Armstrong, R.W., Coffey, C.S., and Elban, W.L. *Acta Met.*, 30, 2111 (1992).

Asaro, R.J., and Needleman, A. *Scripta Metallurgica*, 18, 429 (1984).

Bai, Y. In *Shock Waves and High-Strain-Rate Phenomena in Metals: Concepts and Applications*, (M.A. Meyers and L.E. Murr, eds.) Plenum, New York, 227 (1981).

Balchan, A.S. *J. Appl. Phys.* 34, 241 (1963).

Banks, E.E. *J.I.S.I.*, 206, 1022 (1968).

Barker, L.M. and Hollenbach, R.E. (1974) *J. Appl. Phys.* 45, 4872 (1974).

Beatty, J.H., Meyer, L.W., Meyers, M.A., and Nemat-Nasser, S. in *Shock-Wave and High-Strain-Rate Phenomena in Metals*, (M.A. Meyers, L.E. Murr, K.P. Staudhammer eds.), Marcel Dekker, New York, p. 645 (1992).

Bose, A., Sims, D., and German, R.M. *Met. Trans.*, 19A, 487 (1988).

Brace, W.F., and Bombolakis, E.G. *J. Geophys. Res.*, 68, 3709 (1963).

Broberg, K.B. *Arch. für Fysik*, 18, 159 (1960).

Chang, S.N. and Meyers, M.A. *Acta Met*, 36, 1085 (1988).

Chojnowski, E.A. and McG. Tegart, W.J. *Metals Science Journal*, 1968, 2, 14 (1968).

Christy, S., Pak, H.-r., and Meyers, M.A. In *Metallurgical Applications of Shock-Wave and High-Strain-Rate Phenomena*, (eds. L.E. Murr, K.P. Staudhammer, and M.A. Meyers), Marcel Dekker, New York, p. 835 (1986).

Clifton, R.J. *Material Response to Ultra High Loading Rates*, Report No. NMAB-356, National Materials Advisory Board, NAS, Washington, Chapter 8, 1979.

Clifton, R.J., Duffy, J., Hartley, K.A., and Shawki, T.G. *Scripta Metallurgica*, 18, 443 (1984).

Craggs, J.W. *J. Mech. Phys. Sol.*, 8, 66 (1960).

Curran, D.R. In *Shock waves and Mechanical Properties of Solids*, (J.J. Burke and V. Weiss, eds.), Syracuse University Press, Syracuse New York, p. 121, 1971.

Curran, D.R. and Seaman, L. In *Shock Waves in Condensed Matter* (Y.M. Gupta, ed.), Plenum Press, p. 315, 1986.

Curran, D.R., Seaman, L., and Shockey, D.A. *Physics Reports*, 147, 253 (1987).

Derep, J.L. *Acta Metall.*, 35, No. 6, 1245 (1987).

Dremin, A.N., Molodets, A.M., Melkumov, A.I., and Kolesnikov, A.V. In *Shock-Wave and High-Strain-Rate Phenomena in Materials*, (eds. M.A. Meyers, L.E. Murr and K.P. Staudhammer), Marcel Decker, New York, 751 (1992).

Duvall, G.E. and Fowles, G.R. In *High Pressure Physics and Chemistry*, (edited by R.S. Bradley), Academic Press, New York, **2**, 209 (1963).
Erkman, J.O. *J. Appl. Phys.*, **31**, 939 (1961).
Freund, L.B. *J. Mech. Phys. Sol.*, **20**, 129 and 141 (1972).
Freund, L.B. *J. Mech. Phys. Sol.*, **21**, 47 (1973).
Freund, L.B. *Int. J. Engn. Sci.*, **12**, 179 (1974).
Freund, L.B. *Dynamic Fracture Mechanics*, Cambridge University Press, Cambridge, England (1990).
Glenn, R.C. and Leslie, W.C. *Met. Trans.*, **2**, 2945 (1971).
Goodier, N. *J. Appl. Mech.*, **1**, 39 (1933).
Gourdin, W.H. In *Proc. of Intl. Conf. on Impact Loading and Dynamic behavior of Materials*, Bremen, FRG (1987).
Grady, D.E. *J. Geophys. Res.*, **82-B2**, 913 (1980).
Grady, D.E. *Mechanics of Materials*. In press.
Gray, G.T. In *High-Pressure Shock Compression of Solids*, (J.R. Asay and M. Shahinpoor eds.) Springer-Verlag, New York. In press.
Grebe, H.A., Pak, H.-r., and Meyers, M.A. *Met. Trans.*, **16A**, 761 (1985).
Hartley, K.A., Duffy, J., and Hawley, R.H. *Mechan. Phys. Solids*, **35, No. 3**, 283 (1987).
Hatherly, M. and Malin, A.S. *Scipta Metallurgica*, **18**, 449 (1984).
Hirano, K-I. *Trans. AIME*, **227**, 950 (1963).
Horii, H. and Nemat-Nasser, S. *Trans. Roy. Soc. Lond.* **319**, 337 (1986).
Ivanov, A.G. and Novikov, S.A. *J. Exp. Theor. Phys. (USSR)*, **40**, 1880 (1961).
Johnson, J.N. *J. Appl. Phys.* **52**(4), 2812 (1981).
Kanel, G.I., Rasorenov, S.V., and Fortov, V.E. In *Shock Wave and High-Strain-Rate Phenomena in Materials*, (eds. M.A. Meyers, L.E. Murr, and K.P. Staudhammer), Marcel Dekker, New York 775 (1992).
Krock, R.H. and Shepard, L.A. *Trans. Metal. Soc. AIME.* **227**, 1127 (1963).
Kuriyama, S., and Meyers, M.A. *Met. Trans. A*, **17A**, 443 (1986).
Lankford, J. *J. Mater. Sci.*, **12**, 791 (1977).
Lankford, J., Anderson, C.E. Jr., and Bodner, S.R. *J. Mat. Sci. Lett.* **7**, 1355 (1988).
Leslie, W.C. In *Metallurgical Effects at High Strain Rates* (R.W. Rohde, B.M. Butcher, J.R. Holland and C.H. Karnes, eds.) Plenum Press, New York, 1981.
Louro, L.H.L. and Meyers, M.A. *J. Matls. Sci.*, **24**, 2516 (1989).
Louro, L.H.L. and Meyers, M.A. In *Shock Compression of Condensed Matter—1989*, eds. S.C. Schmidt, J.H. Johnson, and L.W. Davison. Elsevier, New York, 465, 1990.
Marchand, A. and Duffy, J. An Experimental Study of the Formation Process of Adiabatic Shear Bands in a Structural Steel," Brown University Report, April, 1987.
Mescall, J.F. and Rogers, H. MLT TR 89-104, U.S. Army Materials Technology Laboratory Report, 1989.
Meunier, Y., Roux, R., and Moureaud, J. In *Shock-Wave and High-Strain-Rate Phenomena in Metals* (M.A. Meyers, L.E. Murr, K.P. Staudhammer eds.), Marcel Dekker, New York, p. 637, 1992.
Meyer, L.W., Kunze, H.-D., and Staskewitsch, E. *Proc. Seventh Internl. Ballistic Symposium*, The Hague-Netherlands, p. 289, 1983.
Meyers, M.A. *Dynamic Behavior of Materials*, J. Wiley, New York, 1994.
Meyers, M.A. and Aimone, C.T. *Dynamic Fracture (Spalling) of Metals*, In *Progress*

in Materials Science, J.W. Christian, P. Haasen, T.B. Massalski, eds. Pergamon Press, **28**, 1983.
Meyers, M.A. and Chawla, K.K. *Mechanical Metallurgy. Principals and Applications*, Prentice-Hall, Englewood Cliffs, New Jersey, p. 510, 1984.
Meyers, M.A. and Guimaraes, J.R.C. *Mat. Sci. Eng.*, **24**, 289 (1971).
Meyers, M.A., Meyer, L.W., Vecchio, K.S., and Andrade, U. *J. Physique IV, Coll. C1*, **1**, C3-11 (1991).
Meyers, M.A. and Pak, H.-r. *Acta Met.*, **34**, 2493 (1986).
Meyers, M.A., Sarzeto, C., and Hsu, C.-Y. *Met. Trans.*, **11A**, 1737 (1980).
Meyers, M.A., Subhash, G., Kad, B., and Prasad, L. *Mechanics of Materials*, **17**, 175 (1994).
Meyers, M.A. and Wittman, C.L. *Met. Trans.*, **21A**, 3153 (1990).
Molinari, A. and Clifton, R.J. *C.R. Acad. Sci. Paris*, 296 (1983).
Murr, L.E. In *Shock Waves and High-Strain-Rate Phenomena in Metals*, M.A. Meyers and L.E. Murr, eds.), Plenum Press, New York, p. 607, 1981.
Nesterenko, V.F., Meyers, M.A., and Cheng, H.C., "Shear Localization in High-Strain-Rate Deformation of Granular Alumina", submitted for publication (1995).
Rabin, H.B. and German, R.M. *Met. Trans.*, **19A**, 1523 (1988).
Ravi-Chandar K. and Knauss W.G. *Intl. J. Fracture*, **25**, 247 (1984a).
Ravi-Chandar K. and Knauss W.G. *Intl. J. Fracture*, **26**, 65 (1984b).
Robbins, J.L., Shepard, O.C., and Sherby, O.D. *J. Iron Steel Institute*, **202**, 804 (1964).
Rogers, H.C. *Materials Behavior Under High Stress and Ultra-High Loading Rates*, J. Mescall and V. Weiss eds., Plenum Press, New York and London, p. 101, 1983.
Seaman, L., Curran, D.R., Erlich, D.C., Cooper, T., and Dullum, O. *Journal De Physique*, **46**, 273 (1985).
Stevens, A.L., Davison, L., and Warren, W.E. *J. Appl. Phys.*, **43**, 4992 (1972).
Tang, N.Y., Niessen, P., Pick, R.J., and Worsick, M.J. *Mat. Sci. and Eng.*, **A131**, 153 (1991).
Teirlinck D., Zok, F., Embury, J.D., and Ashby, M.F. *Acta Met.*, **36**, 1213 (1988).
Thadhani, N.N. and Meyers, M.A. *Acta Met.*, **34**, 1625 (1986).
Thornton, P.A. and Heiser, F.A. *Met. Trans.*, **2**, 1496 (1971).
Uvira, J.L., Clay, D.B., Worthington, P.J., and Embury, J.D. *Canadian Metallurgical Quarterly*, **11**, 439 (1972).
Wingrove, A.L. *J. Aust. Inst. Met.*, **16**, 67 (1971).
Wittman, C.L., Meyers, M.A., and Pak, H-R. *Met. Trans.*, **21A**, 707 (1990).
Wright, W.T. *J. Mech. Phys. Sol.*, **35**, 269 (1987).
Zehnder, A.T. and Rosakis, A.J. *Intl. J. Fracture*, **43**, 271 (1990).
Zener, C. and Hollomon, J.H. *J. Appl. Phys.*, **15**, 22 (1944).
Zurek, A.K. The Study of Dynamic Fracture During Armor-Penetrator Interaction, *Los Alamos Report*, LA-11719-MS (1989).
Zurek, A.K. *Met Trans. A*, **25**, 2483 (1994).
Zurek, A.K. Unpublished research, 1993.
Zurek, A.K., Follansbee, P.S., and Hack, J. *Met. Trans.*, **21A**, 431 (1990).
Zurek, A.K., Frantz, Ch. E., and Gray, G.T. In *Shock-Wave and High-Strain-Rate Phenomena in Metals*, M.A. Meyers, L.E. Murr, K.P. Staudhammer eds., Marcel Dekker, New York, p. 759, 1992.
Zurek, A.K. and Gray, G.T. *J. Physique IV*, **1**, 631 (1991).
Zurek, A.K., Johnson, J.N., and Frantz, Ch. E. *J. Physique*, **49**(3/9), 269 (1988).